Scientific Highlights
Structural Research 2007/2008

(Photo: X-ray image of "Wie die Alten sungen, so zwitschern die Jungen")

Neutron- and synchrotron radiography – two complementary methods for liquid water detection

Christoph Hartnig[1], Philipp Krüger[1], Robert Kuhn[1], Ingo Manke[2]

■ 1 Zentrum für Sonnenenergie- und Wasserstoff-Forschung, Helmholtzstr. 8, 89081 Ulm, Germany

■ 2 Helmholtz-Zentrum Berlin für Materialien und Energie, Glienicker Str. 100, 14109 Berlin, Germany

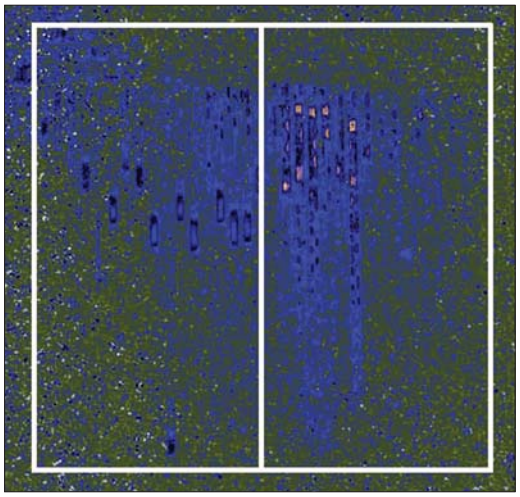

Fig. 1: Neutron radiographic imaging of water transport in an operating fuel cell. The droplet shape has changed caused by different surface properties on the left and right side.

Neutrons are well known for their property to penetrate metallic components almost unattenuated but bear a high sensitivity towards hydrogen containing species; this led worldwide to research activities in fuel cell research, where these two properties are used to optimize performance and durability: liquid water, which forms an obstacle in the transport pathways for the reactant gases, oxygen and hydrogen, has to be detected inside the operating fuel cell, shielded by a metallic housing and other components made of steel or graphite composite materials. Within the last couple of years, synchrotron based methods emerged to a suitable complement in this field to extend the observation scale towards the micrometer level.

Neutron radiography allows for a visualization of the complete electrochemically active area, where the reaction of hydrogen and oxygen takes place and water results as a product. The typically accessible area is in the range of 100-200 cm^2 which agrees well with state-of-the-art fuel cells geometries. The flow field structure, the component of the fuel cell that is responsible for a uniform distribution of the reactant gases, can be optimized that way. Another range of applications focuses on the in situ characterization of the gas diffusion media: the porous media ensures the transport of the reactants to the catalyst particles and of product water from the catalyst to the gas channel where it is removed from the cell. Issues such as impregnation or structural properties influence the liquid water transport and have a significant impact on the performance. In Figure 1 an example of two materials with varying impregnation composition is given: the left material leads to larger droplets and an improved release of the droplets from the surface compared to the material on the right part.

Due to resolution limitations of around 50 µm, only the formation of larger water droplets can be investigated by means of neutron based methods.

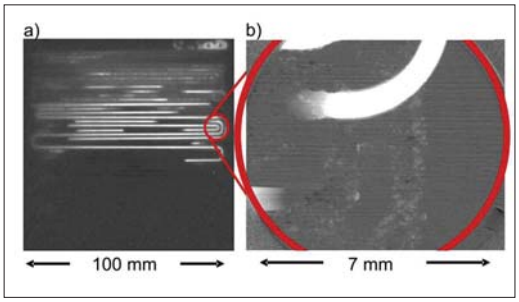

Fig. 2: Complementary character of neutron and synchrotron based methods.

Complementary results can be obtained by synchrotron radiography: as demonstrated in figure 2, the resolution is increased by almost two orders of magnitude allowing for a detection of the initial evolution of small water clusters which has been successfully reported for the first time by our group.

A pseudo three-dimensional and therefore very detailed insight in a fuel cell under operating conditions results from different viewing directions.

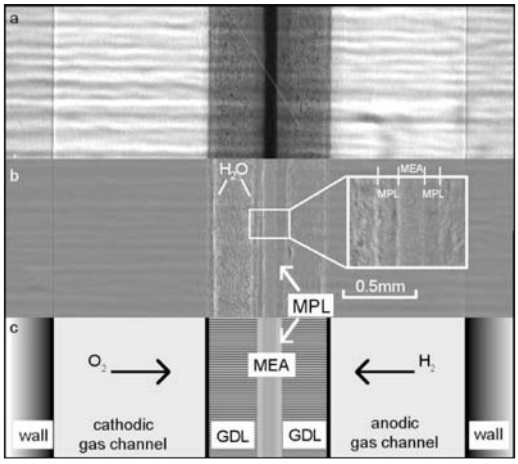

Fig. 3: Cross-sectional viewing direction. a) Uncorrected image, b) After normalization with respect to an 'empty cell', c) Components

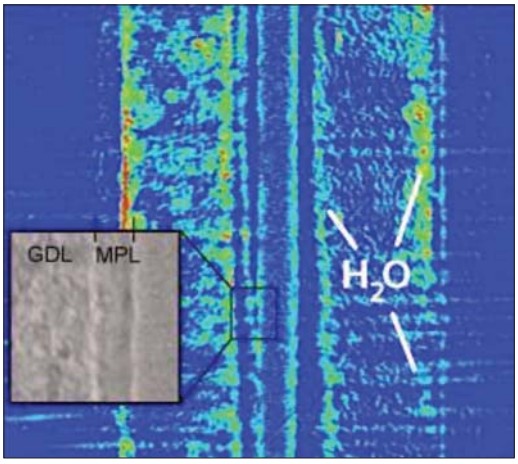

Fig. 4: Transport pathways can be observed from the catalyst layer through the gas diffusion layer (GDL) to the gas channel.

The layers of different components are visible on images in the cross sectional viewing direction, as shown in figure 3. In a further magnification, figure 4, the water distribution and transport processes in the fuel cell assembly can be observed and liquid water can be quantified in the different components. The applied methods were engaged to visualize these effects in a so far unique temporal and spatial resolution. In addition, the through plane viewing direction allows for insights in the specific spots of primary liquid water evolution which are of major interest in an operating fuel cell, the areas under the lands and the channels of the gas distributing flow field. In figure 5, water cluster are detected at different points in the cell. The gas channels are traced in grey and black. At point 1 a water droplet is observable located next to the channel wall. The origin of this droplet is situated at point 2 in the area under the rib, which is free of water in this image. At point 3 liquid water clusters under the rib are detected without droplet generation.

The combination of both viewing directions has been chosen in order to get a pseudo-3D insight in processes on a microscopic scale. An overlay of both aspects allows for an estimation of the total area involved in the liquid water formation and serves as essential input to build and verify multiphase models; development aspects with regard to optimal shape and properties of the employed components can be also addressed.

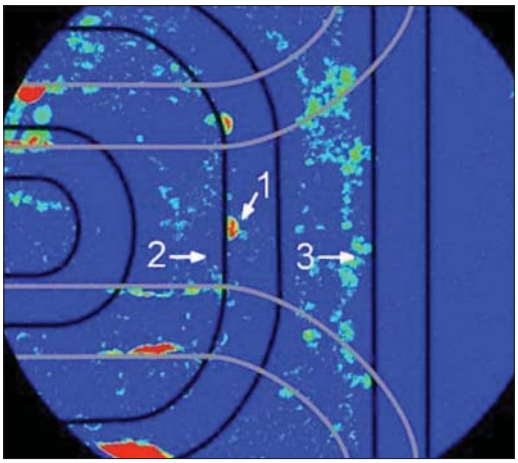

Fig. 5: Liquid water formation rendered visible in the through plane viewing direction: 1) in a gas channel, 2) under the rib next to the channel, and 3) under the rib without direct contact to the gas flow in the channels.

Corresponding authors:
Ingo Manke
manke@helmholtz-berlin.de

Pore network organisation in hierarchical mesoporous silica studied using a combination of gas physisorption with SANS

Simone Mascotto[1], Dirk Wallacher[2], Astrid Brandt[2], Thomas Hauss[2], Bernd M. Smarsly[1]

■ 1 Institute of Physical Chemistry, Universität Giessen, Heinrich-Buff-Ring 58, 35392 Giessen, Germany

■ 2 Helmholtz-Zentrum Berlin, Glienicker Straße 100, 14109 Berlin, Germany

In the past years significant progress has been made in the characterisation of ordered mesoporous materials (pore size between 2 and 50 nm). Standard analytical methods, like small-angle scattering (SAS) and physisorption can be successfully applied to the study of their structural and morphological features (e.g. specific surface area, pore volume and pore size). Although these techniques are widely applied, additional independent experimental methods can be useful especially in the understanding of the sorption mechanism. Recently, the combination of a physisorption experiment with small-angle neutron scattering (in-situ sorption-SANS) was introduced at Helmholtz-Zentrum Berlin (HZB) to provide more details about the porosity and connectivity, which cannot

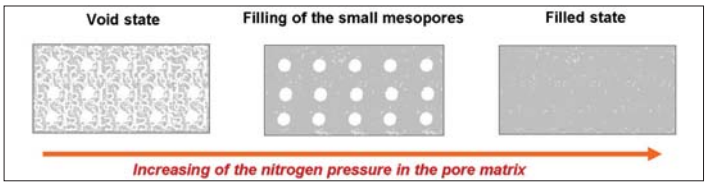

Fig. 1: Scheme of the nitrogen filling in mesoporous silica from "the point of view" of a neutron

be obtained by the single methods themselves. Recently, the use of this combination technique has given relevant results on sorption theory and represents an elegant way to describe the physisorption process in mesoporous materials. [1,2].

The system object of our study is a "hierarchical" mesoporous silica (KLE-IL) which presents a trimodal pore size distribution with distinct maxima at around 1.3 nm, 2-3 nm (cylindrical/worm-like mesopores) and 14 nm (spherical mesopores). We define a "hierarchical" pore system as a pore architecture with the small pores being located in the walls of the larger ones. A considerable amount of microporosity is present in such materials, in addition to the ordered mesoporosity arising from the templating action of the KLE block-copolymer (producing 14 nm spherical mesopores) and of the surfactant-like C_{16}mimCl ionic liquid (generating 2-3 nm cylindrical mesopores) [3].

The SANS experiment involves in-situ nitrogen adsorption at 77 K. The experiment is based on the principle of "contrast matching", with the scattering lengths of the amorphous KLE- silica matrix ($3.43*10^{10}$ cm^{-2}) and condensed nitrogen ($3.22*10^{10}$ cm^{-2}) being almost identical, and thus negligible scattering contrast is present in the filled state [2-4].

In these investigations the relative vapour pressure $p/p°$ of the pore condensate could be controlled during the scattering experiment ($p°$ is the saturation vapour pressure of the bulk condensate at the given temperature). The gas adsorption sample environment (CGA-PT) allows the direct in-situ measurement of a complete pV isotherm. Some of these results are shown in Figure 1, which represent crucial adsorption states of the sorption process (i.e., micropore filling and small mesopores, nitrogen condensation in the larger mesopores). In this context, the essential advantage of the contrast matching conditions is shown, in that filled pores do not contribute to the SANS pattern of the mesopore structure. Therefore, this method is highly sensitive to the pore structure and pore connectivity and perfectly suited to proving the hierarchical order of the KLE-IL porous silica.

The SANS curves (Figure 2), collected at different pressure steps, show various interesting features regarding the porosity and the filling process. First, the pressure-dependent experiments proved that

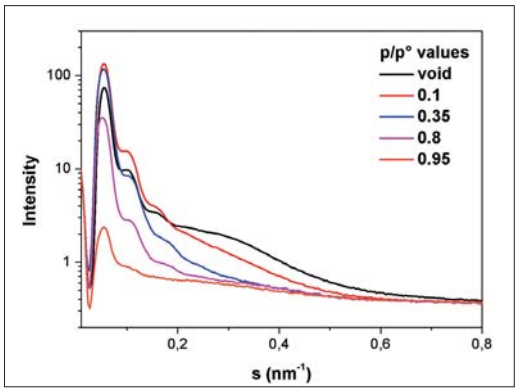

Fig. 2: SANS curves during nitrogen condensation in KLE-IL silica

the SANS data themselves could be attributed to a superposition of three different types of pores. At $p/p° = 0$, the shape of the curve $s<0.25$ nm^{-1} was attributable to the 14 nm KLE mesopores and (based on the relative pressures at which these scattering contributions disappeared) the broad maxima at $s = 0.55$ nm^{-1} and $s = 0.3$ nm^{-1} were assigned to the micropores and small IL mesopores, respectively. Interestingly, at $p/p° > 0.35$, further oscillations corresponding to the form factor of the large spherical KLE mesopores, became visible. At $p/p° = 0.95$ the scattering patterns almost vanish implying that all the pores were filled with nitrogen. Second, and more importantly, the relative overall intensity of the SANS curves showed interesting changes as a function of $p/p°$. Starting from $p/p° = 0$, the SANS curve (below $s = 0.15$ nm^{-1}) underwent a significant, continuous overall increase up to $p/p° = 0.3$-0.35, which coincides with the filling of the micropores and small mesopores. This can be explained by the enhancement of the contrast between the empty KLE mesopores and the silica matrix, producing higher intensity of the Bragg peak at $s = 0.08$ nm^{-1}.

Despite interesting outcomes by the gas condensation in the mesopores, the in-situ SANS technique can also be successfully applied in the understanding of the pore emptying mechanism of porous solids. Until now, two main theories have been used to explain this phenomeon: cavitation and pore blocking. However, cavitation (spontaneous nucleation of a bubble) is only predicted and has not yet been experimentally proven.

The pore blocking effect (see Figure 3) is expected to occur if the pore only has access to the external surface through a narrower neck, as in the ink-bottle pore. The wide body of the ink-bottle pore remains filled during desorption, until the narrow neck empties first at a lower vapour pressure. Thus, in a network of ink-bottle pores, evaporation of the capillary condensate is obstructed by the pore necks. The vapour pressure, at which a pore body empties, depends upon the size of the necks, the connectivity of the network, and the state of the neighbouring pores. By contrast, recent studies have suggested that, if the neck diameter is smaller than a certain critical size (~ 5 nm) at a given experimental temperature, desorption from the pore body occurs via cavitation. In this case the pore body can empty by diffusion, while the pore neck remains filled [5].

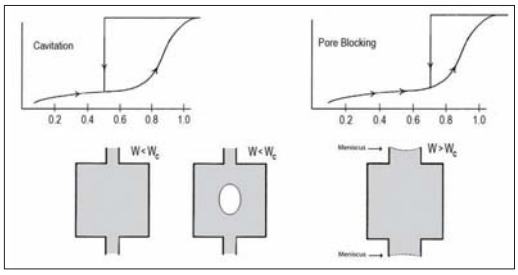

Fig. 3: Scheme of the pore emptying mechanism of cavitation and pore blocking

The use of the in-situ SANS technique offered the unique chance to check the emptying mechanism. The nitrogen desorption at 77K of KLE-IL silica was followed by SANS and is presented in Figure 4. As can be seen, the progressive increase in the intensity of the Bragg maximum at

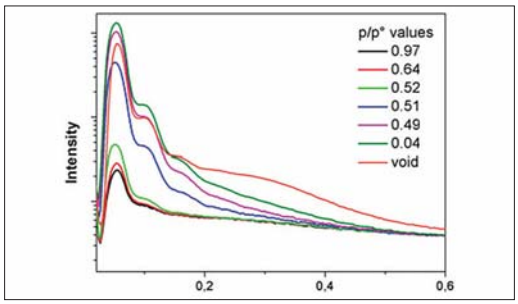

Fig. 4: SANS patterns during the nitrogen desorption branch in KLE-IL silica

$s = 0.08$ nm^{-1} peak for $p/p° = 0.5$, reveals the emptying of the KLE cavities with the IL mesopores still being filled. At smaller relative pressure values ($p/p° < 0.49$) the enhancement of the scattering intensity at $s = 0.3$ nm^{-1} evidences the subsequent draining of the IL mesopores and micropores. This finding is a direct proof of the cavitation pore emptying mechanism.

These first studies give an indication of how this new and elegant approach in the analysis of mesoporous material may provide the answers to many unanswered questions. Furthermore, the in-depth mathematical quantitative investigation of the SANS curves (which was not shown here for the sake of clarity) offer the chance to study the sorption mechanism and its particularities for mesoporous solids in greater detail.

[1] O. Sel, A. Brandt, D. Wallacher, M. Thommes, B. Smarsly Langmuir 2007, 23, 4724-4727
[2] B. Smarsly, C. Göltner, M. Antonietti, W. Ruland, E. Hoinkis J. Phys. Chem. B 2001, 105, 831-840
[3] O. Sel, D. B. Kuang, M. Thommes, B. Smarsly Langmuir 2006, 22, 2311-2322.
[4] E. Hoinkis Part. Part. Syst. Charact. 21 2004 80 – 100
[5] M. Thommes, B. Smarsly, M. Groenewolt, P.I. Ravikovitch, A.V. Neimark Langmuir 2006, 22, 756-764

Corresponding author:
Bernd M. Smarsly
bernd.smarsly@phys.chemie.uni-giessen.de

What neutron autoradiography tells us about Old Masters: The genesis of Jan Steen's *"Wie die Alten sungen, so zwitschern die Jungen"*

Dr. Katja Kleinert[1], Maria Reimelt[2]
■ 1 Helmholtz-Zentrum Berlin für Materialien und Energie, Bereich Strukturforschung, Glienicker Str. 100, 14109 Berlin ■ 2 Gemäldegalerie Berlin, Restaurierungswerkstatt, Stauffenbergstraße 40, 10785 Berlin

Fig. 1: Jan Steen, *"Wie die Alten sungen, so zwitschern die Jungen"*, 1665/66, canvas, 84.8×100.4 cm, Gemäldegalerie Berlin

The Gemäldegalerie Berlin, Stiftung Preußischer Kulturbesitz (Berlin Picture Gallery) and Hahn-Meitner-Institut cooperate closely on investigating paintings by Old Masters by means of neutron autoradiography. This is a very effective, non-destructive, if rather unusual method applied to the examination and analysis of materials and techniques used in painting. It allows the visualisation of structures and layers beneath the surface and, in addition, enables the detailed identification of the elements contained in the pigments. The instrument B8 at Berlin Neutron Scattering Centre (BENSC) is dedicated to these investigations. In this report, the efficiency and success of this method are demonstrated on a painting by the Dutch artist, Jan Steen.

Jan Steen may be considered as one of the most prolific artists of the 17th century. Like many other

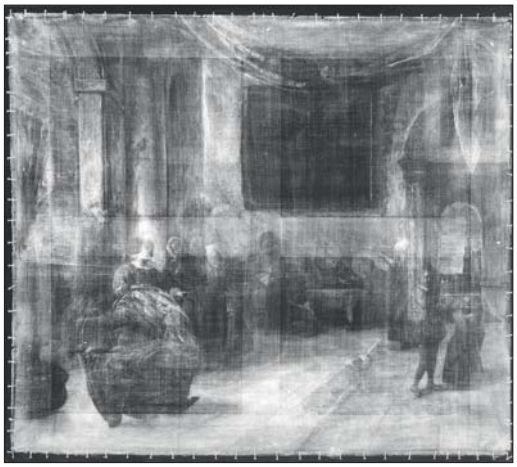

Fig. 2: X-ray image of *"Wie die Alten sungen, so zwitschern die Jungen"*. The X-ray image already shows that large areas of the painting, like the drapery on the upper part or the archway on the right, have been changed during the painting process.

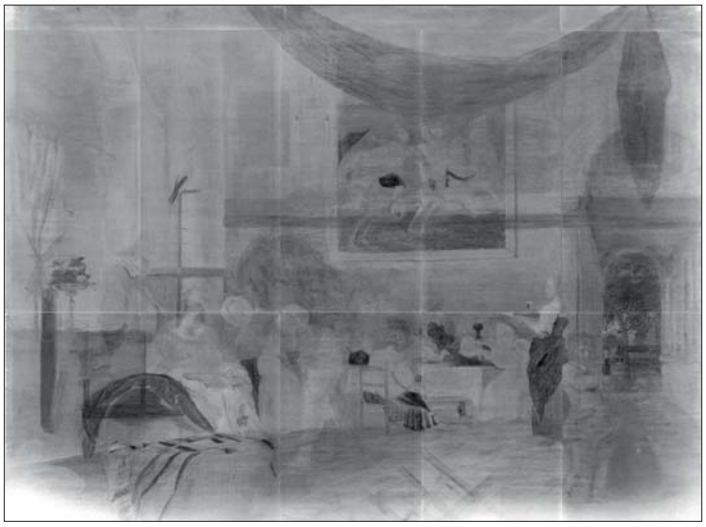

Fig. 3: First neutron autoradiography of *"Wie die Alten sungen, so zwitschern die Jungen"*, depicting clearly the drapery and the landscape in the archway.

painters of that time, he produced several variations on the same theme during his career, following a dedicated scheme of iconographic motives and a defined canon of pictorial elements. The painting *"Wie die Alten sungen, so zwitschern die Jungen"*, roughly translated as "the young cock crows like the old one" or "like mother, like daughter" (Figure 1), which belongs to the Gemäldegalerie Berlin, depicts a topic which Jan Steen addressed in 13 different pictures. However, the Berlin painting is an exception in this series, as it differs in form and content from the other works. Hence the question arises: Why did the artist go to such trouble to deviate from his accustomed paint schemes?

The answer is revealed by X-ray images (Figure 2) and neutron autoradiographies of the painting (Figures 3 and 4). These methods provide insights into paint layers that are hidden today and uncover information about the painter's work process. They show that Jan Steen not only made drastic changes to the composition of the room with regard to the figure groups, but originally had a completely different subject in mind. Most probably, it was a so-called "merry company" in a spacious, stately room. Numerous elements of this original, much more sophisticated ambiance were eliminated by the artist in the version now visible. Essential elements – like the representative arrangement of the room – were retained, but adapted and blended in the composition of the new painting. In this way, Jan Steen integrated the topic *"Wie die Alten sungen, so zwitschern die Jungen"* into a context which was originally designed for a different painting. Apart from revising the composition of the picture, Jan Steen also made essential changes to the iconography of the painting. It can be assumed that these intelligent iconographic alterations were due to the unsuccessful painting process in the first painting: Jan Steen was forced to find the most effective way of using the existing composition if he wanted to save at least a small part of the work already carried out.

Until now, it had not been possible to place the Berlin painting in the chronological order of Jan Steen's oeuvre, especially as he seldom dated his paintings. On the evidence of several characteristic motifs, visible only in the autoradiographies (sometimes just details), and further art historical references, it is now possible to narrow down the date of origin with a high degree of accuracy.

Fig. 4: Second neutron autoradiography of *"Wie die Alten sungen, so zwitschern die Jungen"* with contour drawings of the reconstructed original version.

Corresponding author:
Andrea Denker
denker@helmholtz-berlin.de

Synthesis and cycling behaviour of lithium borohydride

A. Remhof[1], O. Friedrichs[1], Ph. Mauron[1], F. Buchter[1], A. Züttel[1], A. Buchsteiner[2], D. Wallacher[2]

■ 1 Empa - Swiss Federal Laboratories for Materials Testing and Research, Division Hydrogen and Energy, Überlandstrasse 129, 8600 Dübendorf, Switzerland ■ 2 Helmholtz-Zentrum Berlin für Materialien und Energie GmbH, BENSC, Glienicker Strasse 100, 14109 Berlin, Germany

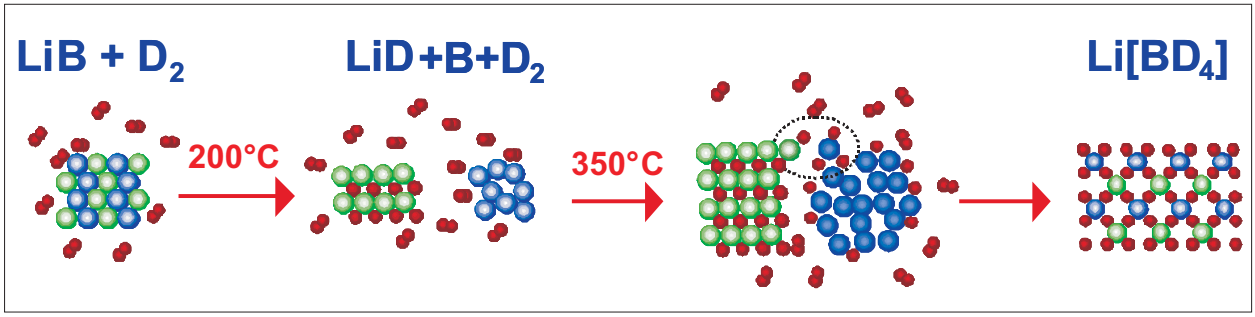

Fig. 1: Schematic view of the $LiBD_4$ synthesis from LiB and D_2.

A future hydrogen economy relies on dense, safe, efficient and reversible hydrogen storage. This can either be achieved by the use of compressed gas, by liquefaction or by solid-state storage. Among these alternatives, metal hydrides and complex hydrides reach the highest volumetric densities, even exceeding that of liquid hydrogen without the need of cryogenic temperatures or high pressures [1,2].

The fundamental properties of a technical applicable hydrogen storage material are (i) a high storage capacity, (ii) fast sorption kinetics and (iii) a convenient working temperature. Due to their combined large volumetric and gravimetric storage capacity, complex borohydrides such as lithium borohydride ($LiBH_4$) are the focus of many research activities world-wide. A major hindrance to their technical applications is their high stabilities, leading to high desorption temperatures. Additionally, the rather slow kinetics of the sorption processes remains a challenge. In view of technical applications, the conditions for the synthesis (i.e. the production) and for the hydrogen cycling (i.e. the hydrogen extraction and refuelling), have to be further improved. Here we present new insights in the synthesis and in the cycling behaviour of $LiBH_4$ gained by in-situ neutron diffraction.

$LiBH_4$ melts at 280°C and decomposes in the liquid phase to LiH, B and H_2 according to the reaction $LiBH_4 \rightarrow LiH + B + 3/2H_2$. The thermodynamic parameters of the desorption have been determined from pressure–composition isotherms according to the van't Hoff law to be $\Delta H = 74$ kJ $(mol\ H_2)^{-1}$ and $\Delta S = 115$ J K^{-1} $(mol\ H_2)^{-1}$, respectively [3]. The reverse reaction, i.e. the synthesis of $LiBH_4$ from it's desorption products requires elevated temperatures (T=600°C) and pressures (p=155bar H_2) [3]. For every day use these values are far too high. We succeeded in reducing the required pressures and temperatures by using pre-annealed Li/B mixtures or AlB_2 and LiH as starting materials. The reactions were monitored in collaboration with the DEGAS laboratory, by combined in-situ neutron diffraction using the focussing diffractometer E6 and gas absorption measurements. ^{11}B was chosen to avoid the strong neutron absorption by ^{10}B that is present in natural boron and D_2 was chosen instead of H_2 to maximise the coherent scattering cross section. We observed the direct, solvent free synthesis of $LiBH_4$ from the elements at 700°C with an applied hydrogen pressure of 150bar. Pre-annealing of Li and B prior to the hydrogen exposure (p=150bar H_2) facilitated the formation [4]. The initial binary compound could be identified as LiB. In a first reaction step the D replaces the B, LiB decomposes and LiD forms. The subsequent synthesis of $LiBD_4$ starts at 350°C, facilitated by the higher reactivity of the B, which is liberated in the decomposition of the binary compound LiB. The resulting reaction scheme is shown in Figure 1 [5]. A further improvement could be reached by using AlB_2 and LiH as starting materials. The synthesis would follow the reaction $AlB_2 + 2LiH + H_2 \rightarrow 2LiBH_4 + Al$. Again, the reactivity of the B liber-

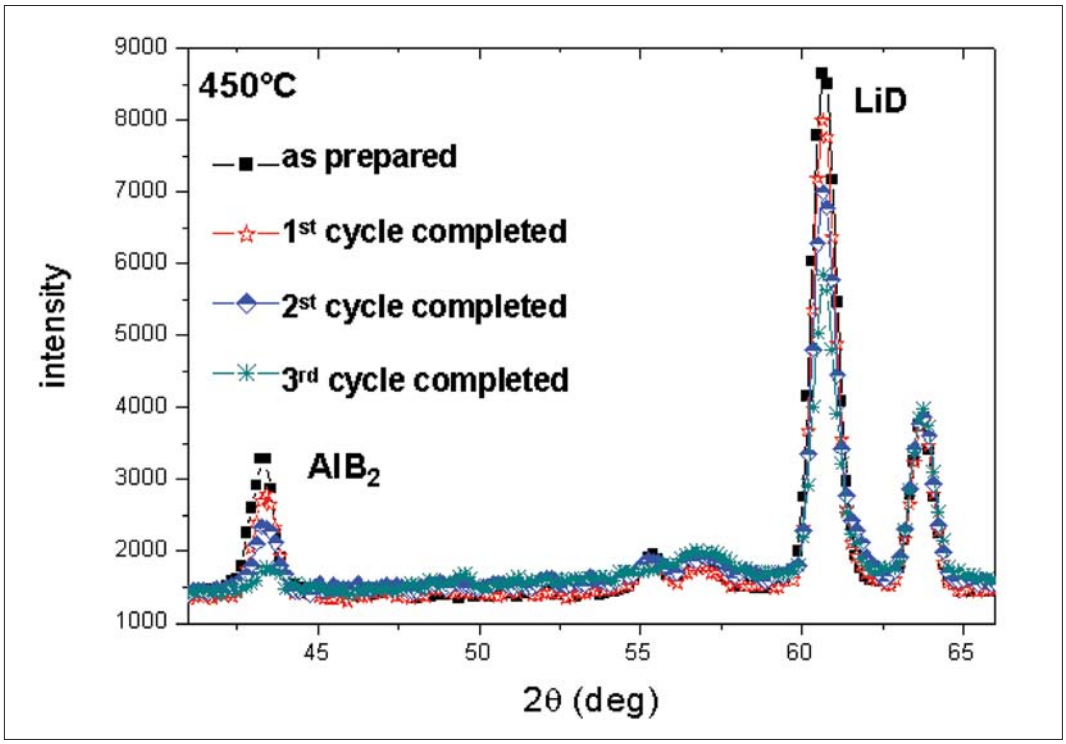

Fig. 2: Cycling of $LiBD_4$ and Al according to $AlB_2 + 2LiH + H_2 \leftrightarrow 2LiBH_4 + Al$, monitored by in-situ neutron diffraction.

ated, this time from AlB_2, facilitates the reaction, which starts at 450°C and at a pressure $\leq$ 25 bar, which is much lower than the pressures reported for the direct synthesis. The presence of Al also improves the cycling behaviour with respect to kinetics and the required pressure and temperature as compared to the pure system. However, the hydrogen capacity decreases from cycle to cycle due to an incomplete re-formation of AlB_2 as shown in Figure 2. We attribute this to a phase separation of Al and B during the decomposition of the $LiBH_4$.
Neutron diffraction helps to reveal the crystalline structure and the reaction path during the hydrogen sorption/desorption cycle of complex metal hydrides. It is hoped that further understanding of the hydrogen dynamics within these systems will be gained in the future by the use of inelastic and quasielastic neutron spectroscopy.

Financial support from the European Commission's 6th Framework Programme (NESSHY Contract No.: 518271), the Swiss National Science Foundation (SNF-Project 200021-119972/1) and the Swiss Federal Office of Energy is gratefully acknowledged. We would also like to thank Norbert Stüßer and Andreas Hoser for their technical and scientific support.

[1] L. Schlapbach and A. Züttel, *Nature*, 414 535 (2001). 414, 535.
[2] G. W. Crabtree, M. S. Dresselhaus and M. V. Buchanan, *Phys.Today*, 39 57 (2004).
[3] Ph. Mauron, F. Buchter, O. Friedrichs, A. Remhof, M. Bielmann, C. N. Zwicky, A. Züttel, *Phys. Chem*. B 112 906 - 910 (2008).
[4] O. Friedrichs, F. Buchter, A. Borgschulte, A. Remhof, C.N. Zwicky, Ph. Mauron, M. Bielmann, A. Züttel, *Acta Mater.* 56 (5), 949-954 (2008).
[5] A. Remhof, O. Friedrichs, F. Buchter, Ph. Mauron, A. Züttel and D. Wallacher, *Phys. Chem. Chem. Phys.* 10, 5859–5862 (2008).

Corresponding author:
A. Remhof
arndt.remhof@empa.ch

Uptake of 1.4 nm versus 18 nm Gold particles by secondary target organs is size dependent in control and pregnant rats after intratracheal or intravenous application

M. Semmler-Behnke[1], S. Fertsch[1], G. Schmid[2], A. Wenk[1], W.G. Kreyling [1]

■ 1 Helmholtz-Zentrum München - Deutsche Forschungszentrum für Gesundheit und Umwelt, Institut für Inhaltationsbiologie, Neuherberg, München, Deutschland ■ 2 Universität Duisburg-Essen, Institut für Anorganische Chemie, Essen, Deutschland

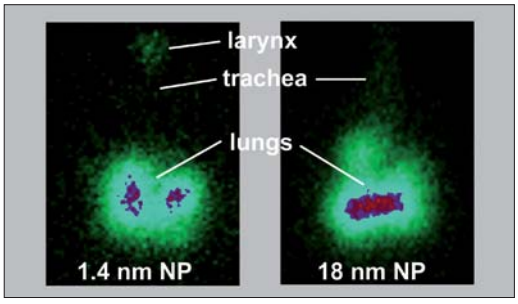

Fig. 1: SPECT gamma camera (Prism 2000, Philips) image of 198Au activity distribution (applying pinhole collimation geometry) in the lungs of animals 1 h after intratracheal instillation of 1.4 nm and 18 nm NPs.

With the advent of nanotechnology, the interaction of nanoparticles (NPs) and nano-structured surfaces with biological systems (including living cells) has become one of the most intriguing areas of basic and applied research at the interface of biology. As NPs are of the same size scale as typical cellular components and proteins, such particles are suspected of evading the natural defences of the human body and may lead to permanent cell damage[1]. This includes NP transfer across biological membranes, NP interactions with proteins and cellular constituents as well as the impact of NPs on important biological functions. In order to assess the effects of NPs, potential target organs and cells need to be known[2]. Target organs may not be restricted to the organ of intake but may include secondary target organs and their cellular constituents, depending on the accessibility of NPs to these sites. Since the interest in gold (Au) NPs continues to grow in nanobiotechnology we selected these for our biokinetic studies[3-5]. We aimed to investigate the effect of the size of monodispersed NPs, keeping the NP material and its ionic ligand coating constant. We compared 1.4 nm sized gold NPs[6-8] with 18 nm gold NPs[9], both stabilised by negatively charged ionic ligands in aqueous solution and radio-labelled with 198Au. Healthy adult Wistar-Kyoto (WKY) rats received radio-labelled gold either by an intratracheal (IT) route or intravenously (IV) in 50 µl of physiological saline in the tail vein. After NP administration, images were taken under a single photon emission computed tomograph gamma camera (SPECT, Prism 2000, Philips), equipped with a pinhole collimator. Rats were killed 24 hours after administration and all organs and tissue samples as well as the remaining carcass, urine and faeces were analysed quantitatively by gamma-spectrometry. The biokinetics in rats after NP administration were compared in two important organs of intake, the lungs and the blood.

These biokinetics in-vivo studies were conducted in healthy, adult female WKY rats (~250g body weight) and performed under German federal guidelines for the use and care of laboratory animals and were also approved by the responsible regional authorities (Regierung von Oberbayern, Approval No. 211-2531-94/04) and by the GSF Institutional Animal Care and Use Committee.

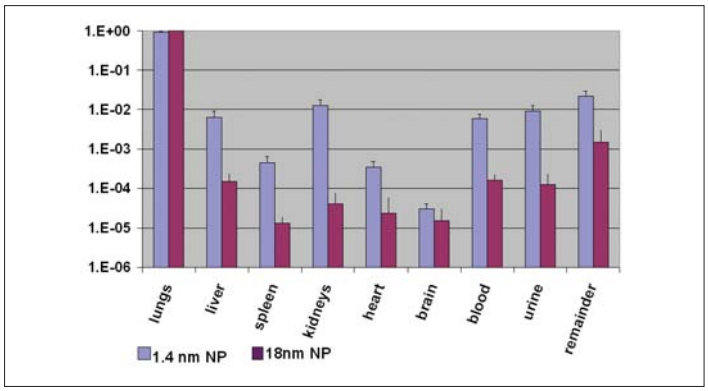

Fig. 2: Translocated NP fractions in secondary target organs 24 h after particle instillation into the lungs (data are corrected for fast clearance).

Twenty-four hours after IT administration, there was considerable retention of NPs in the lung, at both particle sizes. After correction for fast clearance

(the amount of particles which were deposited in the upper airways and cleared via the mucociliary escalator within 24 h) more than 90 % of the administered particles remained on the lung surface (see Figures 1 and 2).

We found a highly significant inverse size dependency with more than a 20-fold higher accumulation of 1.4 nm NPs in secondary target organs (0.039 fraction versus 0.0018 for 18 nm NP ($p<0.001$)). With correction of the particle fraction for fast clearance we found 7% of 1.4 nm NPs translocated into the circulation and to secondary organs, with a 25-fold less translocation for 18 nm colloids. Similarly, the 0.006 fraction of 1.4 nm NPs circulating in blood was 30-fold higher than the 0.0002 fraction for 18 nm NPs. In almost all secondary target organs, translocated fractions of 1.4 nm NPs are mostly up to 2 orders of magnitude larger than for 18 nm NPs (see Figure 2).

Twenty four hours after intravenous injection, the fraction of circulating 1.4 nm NPs in blood (0.037) was 130-fold higher than that of 18 nm NPs (0.00027). This shows that more than 0.96 and 0.99 of the fractions respectively had been taken up by secondary target organs. However, only 0.49 of the 1.4 nm NP fraction was retained in the liver versus 0.94 for 18 nm NPs. Hence, a much larger fraction of the 1.4 nm NPs was distributed in the other organs and tissues compared to 18 nm NPs (see Figures 3 and 4). In the remaining carcass (including muscles and skeleton), we found a 0.16 fraction versus 0.020 for 1.4 nm and 18 nm

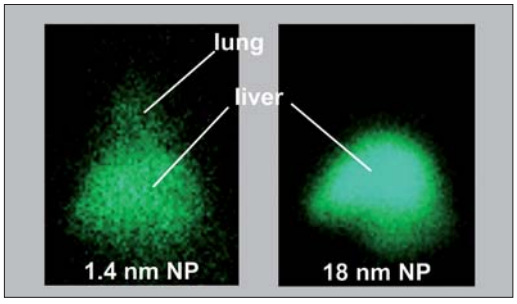

Fig. 3: SPECT gamma camera (Prism 2000, Philips) image of ^{198}Au activity distribution (applying pinhole collimation geometry) 1 hour after intravenous injection of 1.4 nm and 18 nm NPs.

NPs respectively. In addition, a remarkable fraction (0.057) of the 1.4 nm NPs was excreted in the urine, 1000-fold higher than for the 18 nm NPs. Interestingly, a considerable fraction of both 1.4 nm and 18 nm NPs were found in the gastrointestinal tract and faeces, 0.051 and 0.014 respectively. We hypothesise that the excreted fraction was predominantly associated with NPs coming from the liver via the bile and entering the small intestine, thus indicating a strong inverse size dependence of this

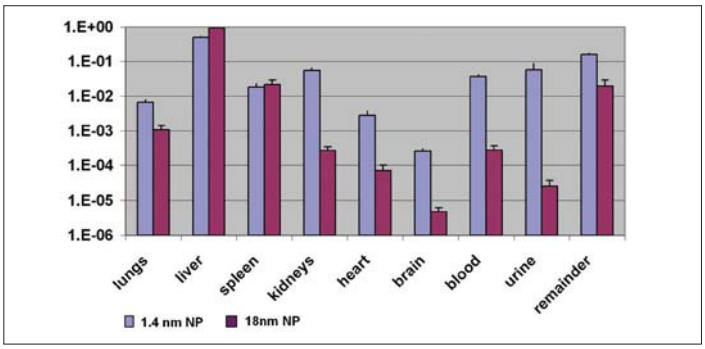

Fig. 4: Translocated NP fractions into secondary target organs 24 h after intravenous injection of the NPs into the tail vein.

clearance mechanism. In the secondary target organs (kidneys, heart and brain) we found about 100-fold more of the 1.4 nm NP fraction compared to the 18 nm NP fraction (see Figure 4).

Twenty-four hours after IV-injection of either sized gold NPs in pregnant rats we found a strong and size-dependent uptake of these NPs by the placenta (about 3% of 1.4 nm NPs and about 0.02% of 18 nm NPs) and thereby also in the foetus (0.06% and 0.005% respectively).

Conclusion: By using NPs of differing sizes but with the same NP matrix, these experiments show that the size of the gold NPs clearly affects translocation kinetics across the alveolar air-blood barrier and vascular endothelium. Potential adverse health effects in secondary target organs require further investigation.

[1] Oberdörster, G.; Oberdörster, E.; Oberdörster, J. *Environ Health Perspect* 2005, 113, (7), 823–839.
[2] Maynard, A. *Nano Today* 2006, 1, (2), 22.
[3] Chithrani, B. D.; Ghazani, A. A.; Chan, W. C. *Nano Lett* 2006, 6, (4), 662-8.
[4] Tkachenko, A. G.; Xie, H.; Coleman, D.; Glomm, W.; Ryan, J.; Anderson, M. F.; Franzen, S.; Feldheim, D. L. J Am Chem Soc 2003, 125, (16), 4700-1.
[5] Tkachenko, A. G.; Xie, H.; Liu, Y.; Coleman, D.; Ryan, J.; Glomm, W. R.; Shipton, M. K.; Franzen, S.; Feldheim, D. L. Bioconjug Chem 2004, 15, (3), 482-90.
[6] Schmid, G. *Inorg. Syntheses* 1990, 7, 214.
[7] G. Schmid, N. K., L. Korste, U. Kreibig, D. Schönauer. *Polyhedron* 1988, 7, 605.
[8] G. Schmid, R. B., R. Pfeil, F. Bandermann, S. Meyer, G. H. M. Calis, J. W. A. van der Velden,. *Chem. Ber.* 1981, 114, 3634.
[9] J. Turkevitch, P. C. S., J. Hillier. *Discuss. Faraday Soc.* 1951, 11, 55.

Corresponding author:
M. Semmler-Behnke
Manuela.Behnke@gsf.de

Magnetism at Single Isolated Iron Atoms Implanted in Graphite

R. Sielemann[1], Y. Kobayashi[2], Y. Yoshida[3], H.P. Gunnlaugsson[4], G. Weyer[4]

■ 1 Helmholtz-Zentrum Berlin für Materialien und Energie ■ 2 Institute of Physical and Chemical Research (RIKEN), Japan ■ 3 Shizuoka Institute of Science and Technology, Japan ■ 4 Department of Physics and Astronomy, University of Aarhus, Denmark

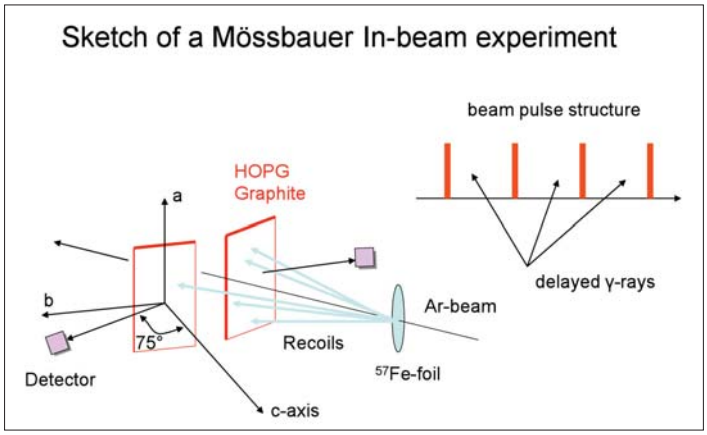

Fig. 1: Sketch of the 'In-Beam-Mössbauer-Spectroscopy' technique. A high energy Ar beam entering from the right excites and implants ^{57}Fe atoms into HOPG samples situated to the left and right of the beam. The principle of the pulsed beam is also shown.

Magnetism is caused by the spontaneous ordering of magnetic moments caused by some kind of exchange interaction. Typically, atoms with unfilled 3d or 4f shells are at the heart of magnetic materials. However, in the last two decades, organic materials have been found which, under certain conditions, might become magnetic by cooperation of electrons without the presence of the classical magnetic atoms. One particularly interesting material is carbon, in its various allotropic forms, for which indications of magnetic order have been reported in a number of recent publications [1]. This is surprising since carbon tends to form covalent bonds with spins usually paired. Amongst other explanations, defects and unusual structural modifications have been suspected of leading to magnetic structures [1].

We have performed experiments employing Mössbauer spectroscopy to study the geometric and electronic structure and possible atomic diffusion of implanted ^{57}Fe atoms in various carbon structures: diamond, fullerenes and graphite. Since Fe atoms are practically insoluble in these carbon structures a special technique for performing the Mössbauer effect was employed: In-Beam Mössbauer-Spectroscopy [2]. With this technique the ^{57}Fe atom is implanted at high energies (several MeV) and, at the same time, the Mössbauer active state is excited by Coulomb excitation without employing a radioactive precursor. In this way the whole experiment is performed on the 100 nanosecond timescale of the Mössbauer state and no clustering or out-diffusion of the Fe can occur; the concentration of ^{57}Fe atoms is extremely small at about 10^{-15} cm^{-3}. The salient feature of such implantation experiments is a high density of defects of about 1 at. % around the Mössbauer probe. Figure 1 shows a sketch of the technique.

The focus of this article is on experiments with graphite in different modifications. Highly-Oriented-Pyrolytic-Graphite (HOPG) material shows a Mössbauer spectrum with a number of lines grouped around zero velocity, which is typical for several implantation induced lattice sites. Surprisingly, part of the spectrum shows a six-line spectral component that is characteristic of a magnetic interaction at the position of the Fe probe atom for temperatures below 40 K (implantation and measuring temperature). The hyperfine field measured is 32.6 Tesla at 14 K, decreasing to 29.8 Tesla at around 40 K and, additionally, the spectrum shows a quadrupole splitting of 1.2 mm/s. Thus, it is clear that this field is not the field of iron metal as no clustering or segregation occurred. The HOPG material with the c-axis oriented perpendicular to the graphite planes allows the direction of the magnetic hyperfine field to be extracted parallel to the c-axis. A spectrum is shown in Figure 2.

The experiments were repeated in HOPG samples from different suppliers with comparable results. The lattice sites acquired in the implantation process cannot directly be inferred from the Mössbauer parameters; however, the isomer shift (electron density) of the magnetic component suggests that the atom is situated interstitially between two graphene sheets. On the other hand, experiments performed with polycrystalline material do not reveal any effects of magnetism, as shown in Figure 3.

It is of course surprising that a single Fe atom in graphite should be in a distinctly magnetic state. To check for possible magnetic impurities present in the samples, analytical experiments were performed by the ERDA (Elastic-Recoil-Detection-Analysis) technique before and after the implantation [3]. It turned out that the atomic concentration

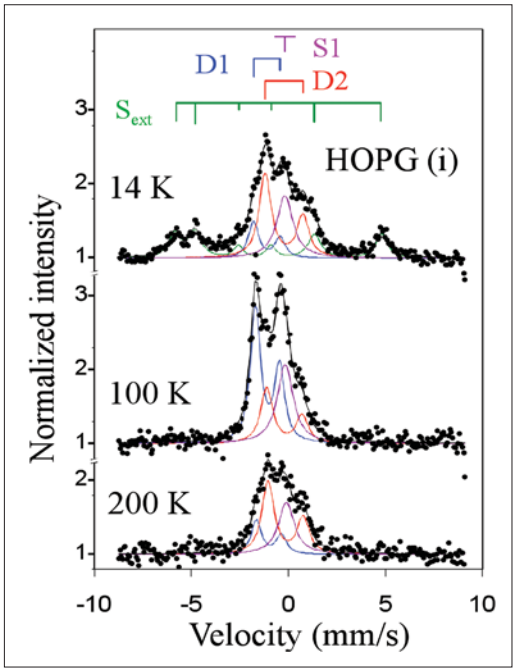

Fig. 2: Mössbauer spectra of ^{57}Fe atoms after implantation in HOPG graphite at the temperatures indicated. The spectra at 100 K and 200 K are fitted with 3 components S1, D1 and D2. Below 40 K, D1 starts converting into the magnetic state S_{ext}.

of all magnetic impurities (e.g. Fe) was smaller than 10^{-5} (before) and around 10^{-4} (after implantation), which is too small to directly produce magnetic effects. Hydrogen impurities amount to 10^{-3} (after implantation). However, the salient feature of the experiments is the large amount of defects, of about 1 at. % from the implantation cascades around the final ^{57}Fe lattice position. A defect density in this range was recently suggested to be sufficient to induce magnetic ordering in several oxides and also in graphite [4]. These calculations show that intrinsic defects (vacancies, interstitials) and certain impurity atoms (like hydrogen) carry magnetic moments and that a realistic exchange interaction may be found leading to magnetic ordering. Experimental evidence for magnetic order in graphite following proton irradiation was recently put forward by Esquinazi et al. [5].

In addition to or in combination with topological defects, the damage cascades of the implantation experiments will also introduce electronic disorder. Such disorder might lead to a mixture of sp^2- and sp^3-hybridized atoms cross-linking graphene layers and, under certain conditions, may constitute a spin system capable of forming an exchange-coupled ordered state. The coupling of ^{57}Fe to the topological and/or spin defects then appears as a possible mechanism to establish the observed magnetism. The fact that polycrystalline graphite does not show evidence for a magnetic state is not easily understood – it might be connected to the production process of the materials leading to different electronic properties. In our additional experiments, indications of magnetism have not been observed in either diamond or in the fullerenes.

The possibility that the spectrum is not a fully ordered state, but a paramagnetic state that is stably oriented in space by an exceptionally weak coupling to the lattice, can very likely be excluded from the measured temperature dependence of the hyperfine field strongly pointing to an interpretation in terms of magnetic ordering. However, since we observed the implanted state in a time window of 100 ns after the implantation process and the created defects are subject to thermal motion depending on the ambient temperature, this could in principle be a situation in which a metastable structure is observed. A relevant publication appeared recently by Sielemann et al.. [6].

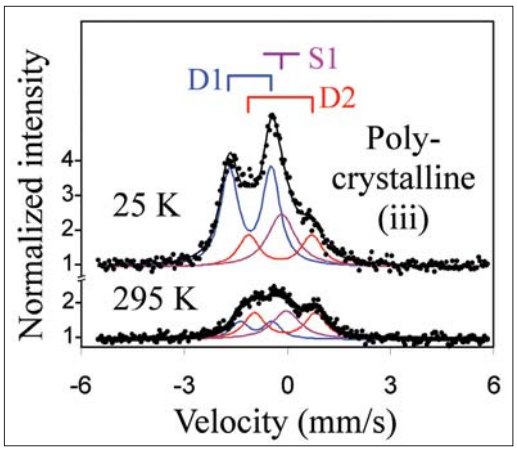

Fig. 3: Mössbauer spectra of ^{57}Fe after implantation in polycrystalline graphite.

[1] T.L. Makarova, Semiconductors 38, 615 (2004).
[2] R. Sielemann and Y. Yoshida, Hyperfine Interact. 68, 119 (1991).
[3] W. Bohne et al., Nucl. Instrum. Methods Phys. Res., Sect. B 136-138, 633 (1998).
[4] P.O. Lehtinen et al., Phys. Rev. Lett. 93, 187202 (2004).
[5] P. Esquinazi et al., Phys. Rev. Lett. 91, 227201 (2003).
[6] R. Sielemann et al., Phys. Rev. Lett. 101, 137206 (2008).

Corresponding author:
R. Sielemann
sielemann@helmholtz-berlin.de

Focusing solid state lens for neutrons

Roland Bartmann[1], Nicolas Behr[1], J. Füzi[2] and Thomas Krist[1]
■ 1 Helmholtz-Zentrum Berlin für Materialien und Energie (HZB), Glienicker Straße 100, 14107 Berlin
■ 2 Budapest Neutron Centre (BNC)

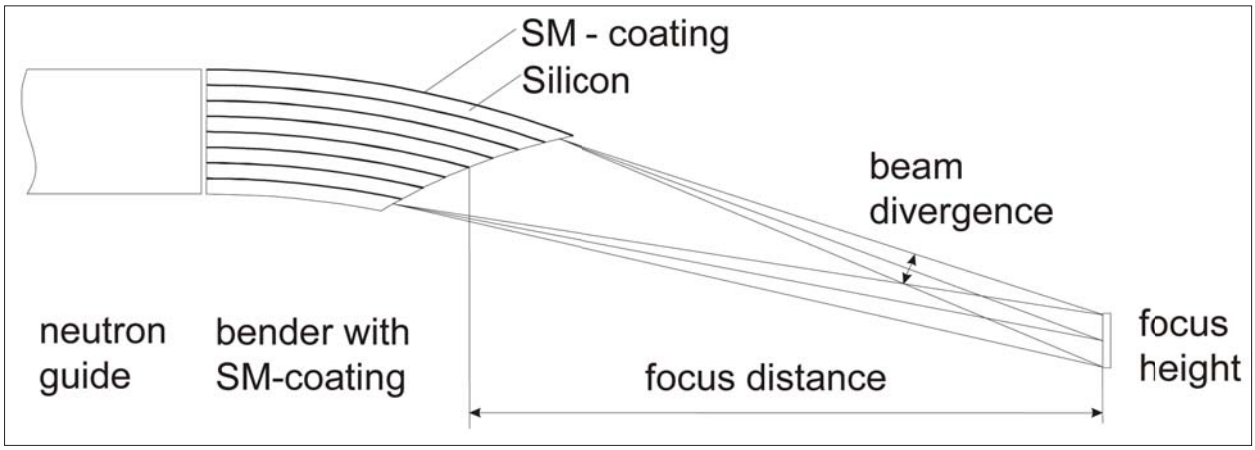

Fig. 1: Asymmetrical focusing lens composed of 100 pieces of 140×20×0.15 mm³ bent silicon wafer with a coating of Ni-Ti supermirrors with m=2. Focus distance 36mm, gain factor 3.4.

In neutron experiments there is always a demand for higher neutron flux at the sample. During the last few years, there has been intensive research in the field of focusing neutrons using refractive lenses, focusing guides, solid state devices, magnetic fields etc.

Given our long experience in building solid state devices we decided to develop a solid state focusing lens. The concept is based on an old idea of Mildner's [1], which was never implemented. It uses a set of curved silicon wafers of different lengths which are coated with reflecting supermirrors. The wafers work as thin guides in which the neutrons follow the curvature of the wafer by means of zigzag or garland reflections. The neutrons are deflected by different total angles depending on the length of the wafers. Since the longer wafers are further away from the beam axis the neutrons travelling in them are more strongly deflected. The curvature and length of the wafers are chosen so that all neutrons meet at a focus a few cm behind the lens. This system accepts the full divergence of a neutron guide if the wafers have the same coating as the guide. Of course, according to Liouville's theorem of

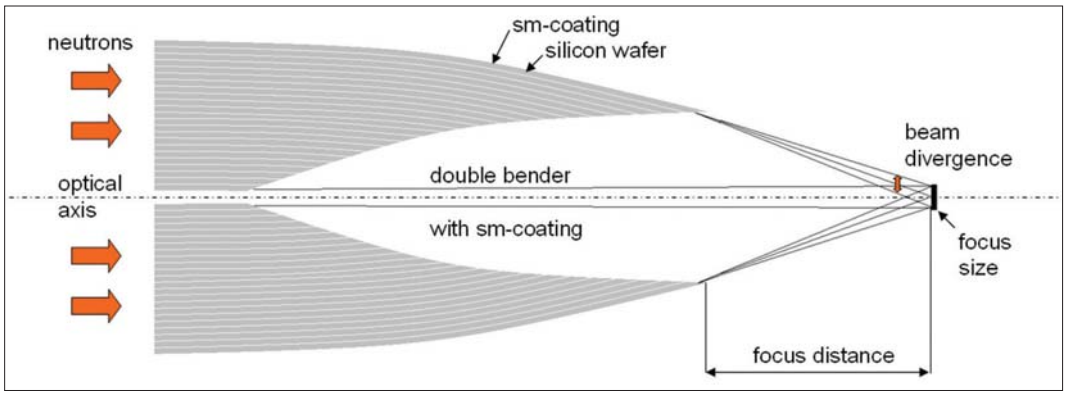

Fig. 2: Symmetrical focusing lens composed of 2×95 pieces of 140×20×0.15 mm³ bent silicon wafer with a coating of Ni-Ti supermirrors with m=2. Focus distance 31mm, gain factor 5.6.

constant phase space density, the increase in intensity in the focus is accompanied by an increase of divergence.

A similar system which also uses thin silicon wafers was built by Johnson and Daymond [2]. However, in this system, neutrons emerging from a point source are refocused to a point focus. However, our system deflects the beam from a guide onto a focal point. As a first step we created such a device consisting of 100 wafers. They were coated by the Budapest group with Ni-Ti supermirrors with m=2, where m gives the ratio of the critical angle of the supermirror to that of nickel. The wafers were bent into a circular shape (Figure 1). This lens was measured with a neutron beam at a wavelength of 4.7Å on the mirror test device V14 at Helmholtz-Zentrum Berlin (HZB). It showed a maximum intensity gain in the focus of 3.4 compared to the direct beam intensity at this position without the lens. The focus was a one dimensional line focus with FWHM of 2.4 mm [3].

The second step was to improve the lens design by using two wafer stacks in a symmetrical arrangement. Each stack consisted of 95 silicon wafers with the dimensions of $140\times20\times0.15$ mm^3 (Figure 2). The lens was measured at V14 and also at the Neutron Tomography Station V7 at HZB, which has a two dimensional photo sensitive detector with submillimetre spatial resolution. The neutron wavelengths were 4.7Å at V14 and 5Å at V7. At V14 a gain of 4.6 [4] and at V7 a gain of 5.6 [5] were measured in the focal maximum. The focus occurred 35mm behind the end of the lens (Figures 3 and 4). This gain implies that more than 40% of all neutrons entering the 31×20 mm^2 entrance window of the lens are focused into the 2.4×20 mm^2 focal line. The remaining neutrons are lost due to attenuation in the silicon and the limited reflectivity of the supermirrors. Measurements at 44 mm and 85 mm behind the focus show a nearly continuous broadening without sharp peaks.

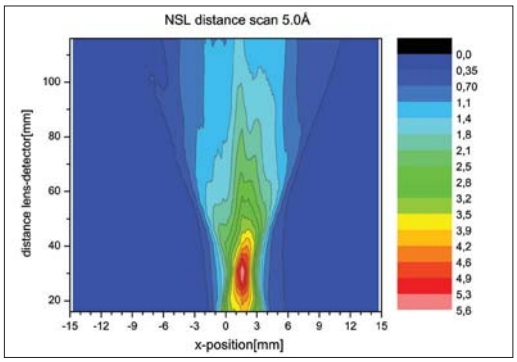

Fig. 4: Contour plot of the intensity gain distribution around the focal spot of the double-sided lens.

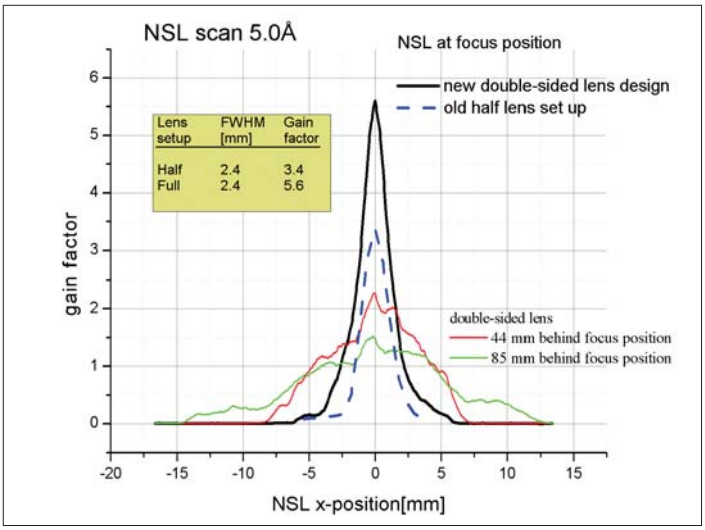

Fig. 3: Gain factor for the symmetric (full lines) and asymmetric (hatched line) lens. The red and green graph give the gain factor at 44 mm and 85 mm behind the focus.

Currently, experiments are underway to show the practical use of the lens in a reflectometer where being able to increase intensity by a factor of 5.6 would be a great advantage.

[1] D.F.R. Mildner: The neutron microguide as a probe for materials analysis, NIM A299 (1990) 416-419.
[2] M.W.Johnson, M.R. Daymond: The neutron silicon lens: a new lens design for thermal neutrons, Physica B283 (2000) 308-313.
[3] Th. Krist, N. Behr, J.-E. Hoffmann: Focusing lens and polarising supermirror, BENSC Experimental Reports 2005.
[4] R. Bartmann, A. Stellmacher, Th. Krist: Improved focusing lens and Nickel/Titanium monochromator, BENSC Experimental Reports 2007.
[5] R. Bartmann, A. Hilger, N. Kardjilov, Th. Krist: Double-sided focusing solid state lens, BENSC Experimental Reports 2007.

Corresponding author:
Thomas Krist
krist@helmholtz-berlin.de

Thermodynamics of the spin Luttinger-liquid in a model ladder material – an example for complementary measurements at LaMMB

K. Kiefer[1] , Ch. Rüegg[2], B. Thielemann[3], D. F. McMorrow[2], D. Biner[4], K. W. Krämer[4]

■ 1 Helmholtz-Zentrum Berlin für Materialien und Energie GmbH, BENSC

■ 2 London Centre for Nanotechnology and Department of Physics and Astronomy, University College London, London WC1E 6BT, United Kingdom

■ 3 Laboratory for Neutron Scattering, ETH Zurich and Paul Scherrer Institut, CH-5232 Villigen, Switzerland

■ 4 Department of Chemistry and Biochemistry, Universität Bern, CH-3000 Bern 9, Switzerland

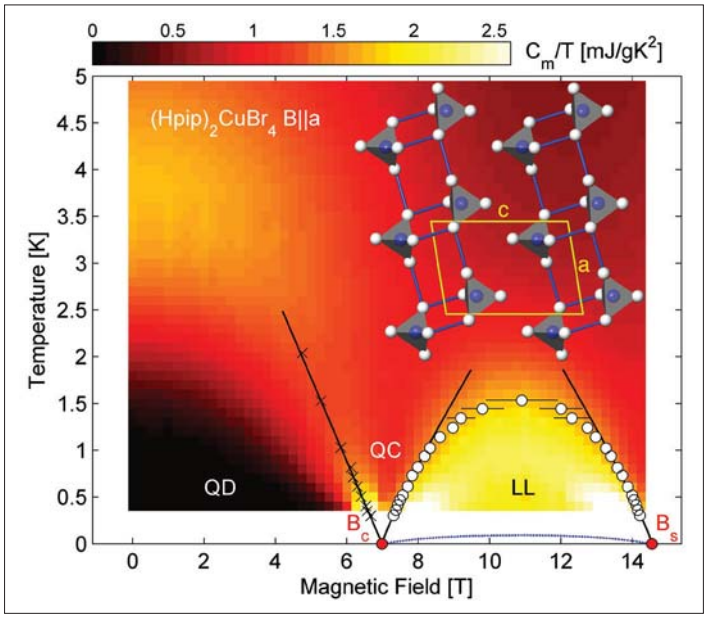

Fig. 1: Field-temperature phase diagram of the spin-ladder compound $(Hpip)CuBr_4$, showing quantum disordered (QD), quantum critical (QC), and spin Luttinger-liquid (LL) phases. The contour plot shows the magnetic specific heat capacity as $C_m(T,B)/T$. Local maxima from the reduction of the triplet gap by the Zeeman effect are indicated by crosses. Circles denote the LL crossover based on measurements of the magnetocaloric effect [Figure 2], black lines are fits to extract the critical fields. The blue line indicates the onset of 3D long-range order below 100 mK [Ref. 3]. Inset: lattice structure of $(Hpip)CuBr_4$ in projection along the b-axis, with Cu atoms blue and Br white.

Quantum spin systems display a remarkable diversity of fascinating physical behaviour such as Bose-Einstein condensation, quantum critical scaling or the Luttinger-liquid regime. One especially interesting model system is the spin ½ two-leg antiferromagnetic ladder, where two quantum phase transitions and the Luttinger-liquid regime can be observed. A quantum phase transition is a phase transition at zero temperature which is driven by an external parameter like, for example, the magnetic field. Unlike a "classical" phase transition where thermal fluctuations play a crucial role, a quantum phase transition is driven by quantum fluctuations. In a spin ½ two-leg antiferromagnetic ladder two quantum phase transitions are to be expected, one from the gapped, dimerised ground state to the Luttiger-liquid regime, and a second from the Luttinger-liquid regime to a field aligned ferromagnetic phase.

However, materials in which to explore such effects are rather rare. Here we present the results of thermodynamic measurements on an exceptional spin ½ two-leg ladder material, the metal-organic compound piperidinium copper bromide $(C_5H_{12}N)_2CuBr_4$, abbreviated as $(Hpip)CuBr_4$ [Ref. 1]. This material is exceptional for two reasons. On the one hand, the complete phase diagram can be explored experimentally with standard laboratory techniques; for this material the critical fields for the two quantum phase transitions are B_c=6.99(5) T and B_s=14.4(1) T. On the other hand, $(Hpip)CuBr_4$ is a nearly perfect representation of a one dimensional spin ½ two-leg ladder with very weak inter-ladder exchange interaction, as determined by inelastic neutron scattering. The exchange interactions are J_{rung}=12.9(2) K and J_{leg}=3.3(3) K with an inter-ladder exchange interaction of J'<100mK [Ref. 2].

In order to explore the phase diagram of (Hpip) CuBr4, heat capacity and magnetocaloric effect measurements were performed on the instrument CM-14.5T of the Laboratory for Magnetic Measurements at BENSC (LaMMB). In Figure 1 the different phases in the phase diagram are identified where a colour plot of the heat capacity divided by the temperature is shown. The most prominent feature is the yellow dome of the Luttinger-liquid regime, where the heat capacity C displays a linear behaviour with temperature T so

that C/T is constant. This behaviour is expected for a Luttinger-liquid. At low magnetic fields and low temperatures the heat capacity decreases exponentially with temperature, revealing the gapped spectrum spectrum of the magnetic excitations.

The white circles in Figure 1 denote the crossover to the Luttinger-liquid regime based on measurements of the magnetocaloric effect. The special technique used at LaMMB for the very accurate determination of the Luttinger-liquid regime boundary is the quantitative quasi-isothermal magnetocaloric effect. With this powerful method it is possible to directly determine the temperature derivative of the magnetisation $\partial M/\partial T|_B$, via the relationship $\partial M/\partial T|_B = -(\delta Q/\delta B)/T$, where δQ is the heat generated in the sample by the magnetocaloric effect at a magnetic field change δB. As the magnetisation M *vs.* temperature T is expected to pass an extremum (maximum or minimum) at the crossover to the Luttinger-liquid regime [Ref. 4], the zero-transition of $\partial M/\partial T|_B$ *vs.*T is indicative of the boundary of the Luttinger-liquid regime. In Figure 2(a) the measured magnetocaloric effect $(\delta Q/\delta B)/T$ is shown for different temperatures. In Figure 2(b) the crossover to the Luttinger-liquid regime is marked by the zero-transition of the magnetocaloric effect (white circles). By the quantitative measurement of the magnetocaloric effect it was possible to detect the Luttinger-liquid regime in a very effective and precise way.

The measured heat capacity data have been compared with numerical calculations of the heat capacity of an ideal spin ½ two-leg antiferromagnetic ladder [Ref. 2]. The measured and calculated heat capacities agree almost perfectly. This agreement reveals again that $(Hpip)CuBr_4$ represents an exceptional model compound for a spin ½ two-leg antiferromagnetic ladder. Hence the material offers unprecedented opportunities to investigate the intrinsic physics of low dimensional quantum systems.

The identification of $(Hpip)CuBr_4$ as an ideal model substance shows the power of combining neutron scattering experiments (partially performed on the BENSC instrument V2) with complementary laboratory-based measurement techniques. This combination of complementary methods was the key for the successful completion of this project.

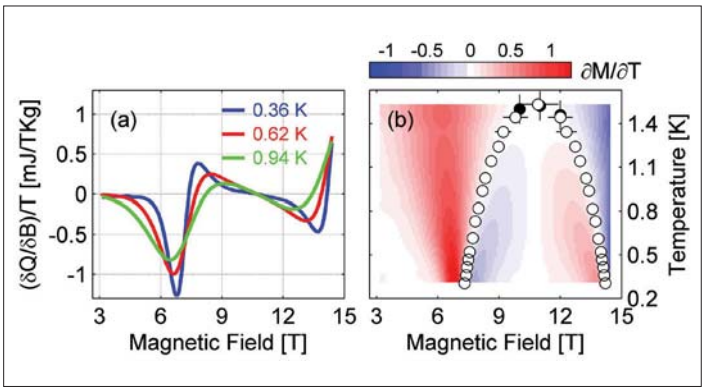

Fig. 2: Magnetocaloric effect in $(Hpip)CuBr_4$. (a) Heat flow δQ to and from the sample as a function of magnetic field divided by temperature, $(\delta Q/\delta B)/T$. (b) Contour plot of $\partial M/\partial T|_B$ as a function of field and temperature. White circles denote the crossover derived from $\partial M/\partial T=0$, while black circles are maxima in the specific heat capacity, obtained at fixed field.

[1] B. C. Watson, V. N. Kotov, M.W. Meisel, D.W. Hall, G. E. Granroth, W. T. Montfrooij, S. E. Nagler, D.A Jensen, R. Backov, M.A. Petruska, G. E. Fanucci, and D. R. Talham, Phys. Rev. Lett. 86, 5168 (2001)

[2] Ch. Rüegg, K. Kiefer, B. Thielemann, D. F. McMorrow, V. Zapf, B. Normand, N. B. Zvonarev, P. Bouillot, C. Kollath, T. Giamarchi, S. Capponi, D. Poilblanc, D. Biner, and K. W. Krämer, Phys. Rev. Letters, Vol. 101, 247202 (2008)

[3] B. Thielemann, Ch. Rüegg, K. Kiefer, B. H. M. Rønnow, B. Normand, P. Bouillot, C. Kollath, E. Orignac, R. Citro, T. Giamarchi, A. M. Läuchli, D. Biner, K. Krämer, F. Wolff–Fabris, V. Zapf, M. Jaime, J. Stahn, N. B. Christensen, B. Grenier, D. F. McMorrow, and J. Mesot, Phys. Rev. B Vol. 79, 020408(R) (2009).

[4] X. Wang and L. Yu, Phys. Rev. Lett. 84, 5399 (2000)

Corresponding author:
K. Kiefer
klaus.kiefer@helmholtz-berlin.de

Dark-field tomography

M. Strobl[1,2], A. Hilger[2], N. Kardjilov[2], I. Manke[2], C. Grünzweig[3], C. David[3], F. Pfeiffer[3]
■ 1 Universität Heidelberg, Germany, ■ 2 SF1/SF3, Helmholtz-Zentrum Berlin für Materialien und Energie, Berlin, Germany, ■ 3 Paul Scherrer Institut, Villingen, Switzerland

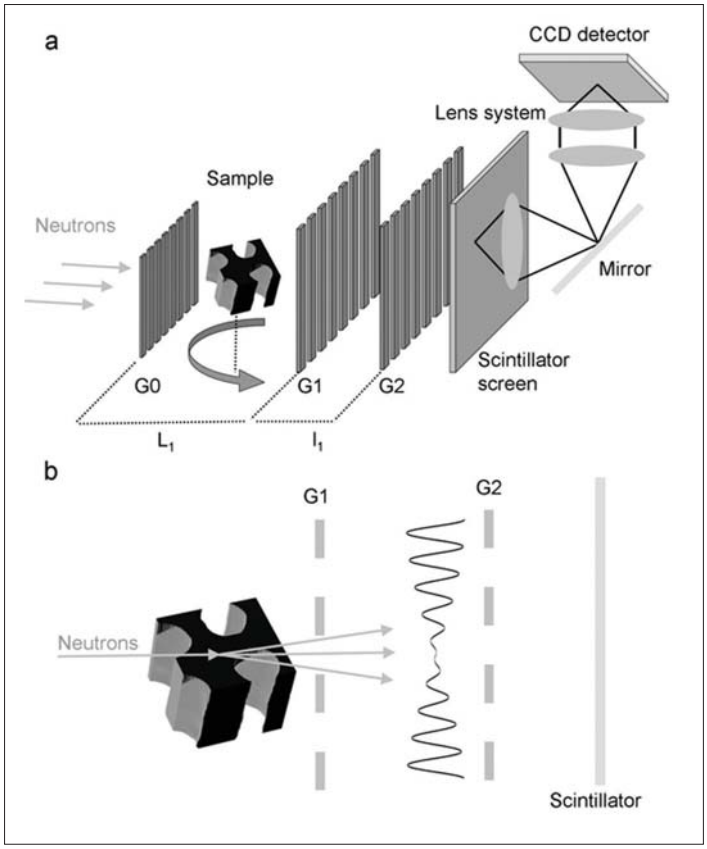

Fig. 1: Grating interferometer (a) Set-up with three gratings, sample and detector system. (b) The visibility of the interference degrades due to ultra-small angle scattering in the sample.

For the last decade, since neutron imaging has been able to profit from digital image recording, it has not only experienced an outstanding gain in importance and applications but also in methodical and technical developments. Besides significant increases in spatial and temporal resolution, new methods are able to address more than the attenuation coefficient conventionally used in order to achieve image contrast and volumetric information about the inner structure of a sample. This means that refractive index distribution, microcrystalline phase and texture, mesoscopic structures causing small-angle scattering, as well as magnetic fields and structures now provide image contrast and can be identified with three-dimensional resolution. The corresponding methods used are phase contrast imaging, energy-resolved imaging at Bragg edges, dark-field (i.e. small-angle scattering) contrast and polarised neutron imaging.

However, some of these methods suffer from severe limitations, such as low flux densities, which hinder their practical application or, in many cases, concerning tomographic application. For phase contrast imaging a grating-based shearing interferometer has been developed recently at Paul Scherrer Institut (PSI). It can be employed to perform differential phase contrast tomographies on reasonable time scales in order to achieve three dimensional reconstructions of the refractive index distribution of a sample [1].

The grating-based shearing interferometer shown in Figure 1 consists of a source grating G0, a phase grating G1 and an analyser absorption grating G2. The absorption source grating with a period p_0 provides a partially coherent beam at the phase grating G1, inducing a phase shift of π with a period of p_1. The analyser grating with a period $p_2 = p_1/2$ at the 1st fractional Talbot distance enables the detection of the interference pattern despite a detector resolution that is at least an order of magnitude too low to resolve the period of the intensity oscillations. A phase stepping approach is applied to resolve the fringe pattern by

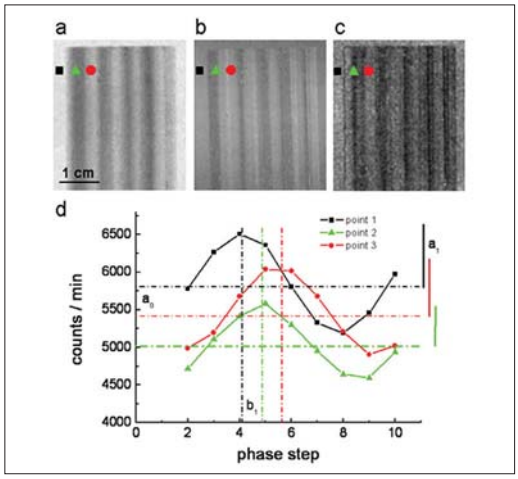

Fig. 2: Radiographic images of an Al sample by (a) attenuation contrast a_0, (b) the differential phase contrast b_1 and (c) the dark-field image a_1. (d) Measured instrumental response function $I = a_0 + a_1 * \cos(b_1)$ for three different image points.

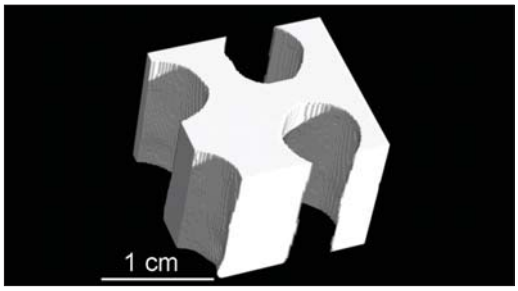

Fig.3: Detail of three dimensional reconstruction of Al sample matrix as derived for each of the three contrast parameters.

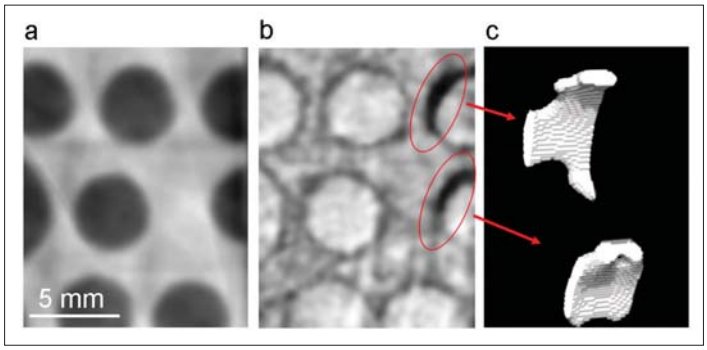

Fig.4: Detail of reconstructed sample cross section in (a) differential phase contrast and (b) dark-field contrast. (c) Extracted three dimensional tomographic reconstruction of sediments found in the dark field contrast images.

recording several images for different scan positions of, for example, the analyser grating. In this way spatial and angular resolution are decoupled and consequently differential phase effects, i.e. refraction, can be detected in spite of relaxed coherence conditions. Analysing the phase shifts of the fringes and the mean intensity over one fringe period for a tomographic measurement provides volumetric reconstructions of the real and the imaginary part (attenuation) of the refractive index distribution.

The novel approach used here is to exploit another parameter for tomography by taking advantage of the grating interferometer. In contrast to differential phase effects, scattering at very small angles does not cause a shift in one direction, but a broadening of the angular intensity distribution [2]. Consequently, it causes a spatial broadening of the maxima of the fringe pattern in the grating interferometer. Indeed, this broadening of the maxima at constant periodic positions reduces the visibility of the fringe pattern (Figure 2). Hence the spatially resolved relative visibility, i.e., the variation of the local amplitude of the fringe pattern is a scattering-related imaging parameter analogous to dark-field imaging or ultra-small angle scattering contrast. The efficiency of this technique means the field of applications can be opened up to include three-dimensional tomographic investigations. Tomographic reconstructions become possible by the extraction of the scattering-induced contribution to the visibility degradation [3] and the formulation of a related Radon transformation. Such Radon tranformation is based on a path integral describing the angular contribution of (multiple) scattering from the sample to the beam divergence, as demonstrated by Strobl et al. [2].

For this purpose a grating interferometer was installed at the CONRAD neutron imaging facility and a reference sample was measured. The tomographic data recorded yielded three dimensional spatially resolved reconstructions of the attenuation coefficient, the real part of the refractive index and the novel dark-field scatter parameter. Although, in this case, all of the contrast signals equivalently recovered the structure of the Al sample matrix (Figure 3), one feature was not displayed in any of them. In some channels of the matrix small sediments could be identified in the dark field reconstruction due to strong scattering at small angles (Figure 4). Since then, the method has been applied successfully to identify, for example, structural inhomogeneities in different Al-Si binary metallic alloys.

Generally, ultra small-angle scattering based reconstructions derived from dark-field images are particularly useful for identifying inhomogeneities caused by structures in objects ranging from about a hundred nanometres to a few micrometres. This range naturally complements the size range that can be spatially resolved by imaging methods. In contrast to the existing crystal analyser-based methods this novel approach allows for three-dimensional dark-field computer tomography on practical time scales. Additionally, the results demonstrate how the tomographic dark-field contrast approach can be applied even at low-brilliant sources, such as state-of-the-art neutron sources or laboratory based x-ray sources. Applications of radiographic dark-field contrast with x-rays have already been reported in various fields, such as medical imaging, food inspection, industrial non-destructive testing and security screening, to name but a few.

[1] F. Pfeiffer et al., Phys. Rev. Lett. 96, 215505 (2006)
[2] M. Strobl et al., Appl. Phys. Lett. 85, 3, 488 (2004)
[3] M. Strobl et al., Phys. Rev. Lett. 101, 123902 (2008)

Corresponding author:
Markus Strobl
strobl@helmholtz-berlin.de

Hydrogen storage in ice

Margarita Russina[1], Ewout Kemner[1], Milva Celli[2], Lorenzo Ulivi[2], Ferenc Mezei[3]
■ 1 Helmholtz-Zentrum Berlin für Materialien und Energie, Berlin, Germany ■ 2 Istituto dei Sistemi Complessi, Sesto Fiorentino Italy ■ 3 SZFKI, Budapest, Hungary

Clathrate hydrates are inclusion compounds, formed by a network of hydrogen-bonded water molecules that are stabilised by the presence of foreign molecules. The hydrophobic interactions between the host framework and guest molecules push the ice to change its structure and form cages of different form and dimensions in order to accommodate the guests. The topology of the ice cages depends on the sizes and shapes of the guest molecules, the typical dimensions of the cages range between 4 - 15Å. The confinement and small size of the cages strongly influence the behaviour of the guest molecules and result in properties that are different from those of the bulk, thus making the clathrate hydrates model system useful in the study of the effects of confinement.

The interest in clathrate hydrates was motivated by their potential as cheap and environmentally friendly energy storage carriers. The synthesis of the hydrogen filled ice clathrates was reported in 2002 by W. Mao [1]. By application of 2000 bar hydrogen pressure she was able to form fully hydrogenated clathrates which are stable up to 160 K under atmospheric pressure and can hold hydrogen at up to 3.77% of the total mass. It has been found that loading pressure can be decreased (to about 300 bar) and the temperature stability can be improved (up to 270 K) by the introduction of large organic molecules into part of the cages of the H_2-clathrates [2].

To discover the reason for these differences we undertook a detailed study of the guest-host interactions using a combined neutron scattering and molecular simulation approach. Guest-host interactions are best reflected in the microscopic dynamics, thus the benefits and complementary nature of neutron scattering and molecular dynamics simulations are obvious: both techniques provide information on atomic trajectories allowing for direct comparison of the theoretical and experimental results. Both methods work with full efficiency on the scale of a few nanometres in length (which is relevant for hydrogen storage structures) and can follow atomic motions on a broad time scale from 10^{-14} to 10^{-10} s.

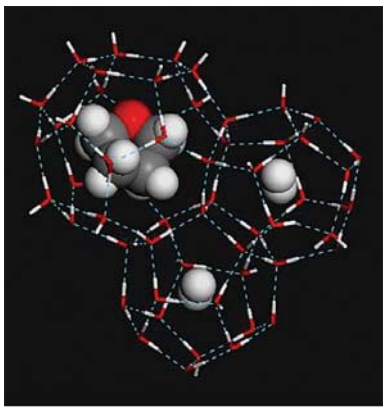

Fig. 1: Structure of ice-based clathrates with small and large cages. Colour coding: red indicates oxygen atoms; grey, hydrogen and dark grey, carbon atoms. The large cage shown in the picture is occupied by a tetrahydrofuran molecule, whilst small cages are occupied by one H_2 molecule each. Note that in H_2-H_2O clathrates, large cages are occupied by two H_2 molecules.

The experimental part of the work has been undertaken using the TOF spectrometer NEAT at the Berlin Neutron Scattering Centre. We investigated the behaviour of molecular hydrogen in the bulk and also confined into cages of ice-based clathrates of differing dimensions. For this purpose we used the composite THF - H_2O - H_2 and H_2O - H_2 systems (THF; tetrahydrofuran). The structure of the H_2 filled ice-clathrates consist from 16 small cavities in the shape of pentagonal dodecahedron (5^{12}) and 8 large cavities in the shape of hexakaidecahedron ($5^{12}6^4$). In the ternary clathrate the THF molecules take up places in the larger cages and the molecular hydrogen only occupies smaller cages (those with an accessible diameter of 5.02Å), with one molecule per cage. In the fully hydrogenated H_2O - H_2 system, hydrogen can occupy both the small and the large cages. These larger cages are of a 6.67Å accessible diameter and accommodate two H_2 molecules per cage (Figure 1).

The scattering function of hydrogen molecules is described by a discrete spectrum of rotational and vibrational levels [3]. The energies of rotational levels are given by $E_{rot}=J(J+1)B$, where $J=1,2,3,\ldots$ and the rotational component is B=7.35 meV. The vibrational levels are given by $E_{vib}=(\nu+ ½)\hbar\omega_{vib}$ with the vibrational constant ω_{vib}=516 meV. The measurements were taken at temperatures in the 2-100 K range.

In the energy range explored on NEAT, the dynamic response of the bulk hydrogen, shows one single peak corresponding to the first rotational transition at 14.7meV. The response changes once the hydrogen is confined to the cages. The first rotational transition splits into three components indicating the anistropic cage environment, the rather weak, Van-der-Walls type interactions between H2 and the ice framework. The splitting in the large cages is greater than that in the small cages indicating the higher anisotropy of the large cages.

However, the surprising feature is that in addition to the first rotational transition, we observed a new additional dynamic feature in 8-12 meV energy

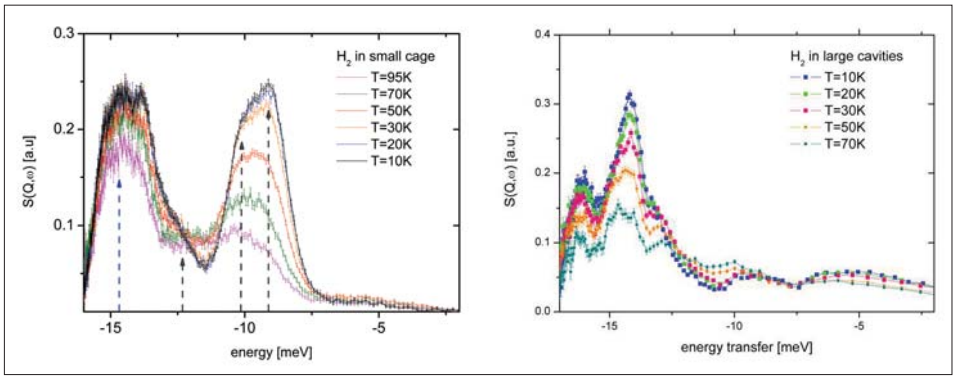

Fig. 2: Dynamic structure factor of hydrogen in small (a) and large (b) cages measured by TOF spectrometer NEAT. Dashed lines indicate the position of first rotational transition in the bulk H2 (black line) and additional modes observed only in the small cage (grey line).

range consisting of several components (Figure 2a). The positions of the peaks are temperature dependent but in different ways: whilst some components soften with increasing temperature, the others exhibit strong anharmonic behaviour and move to the higher frequencies. It is remarkable that such a dynamic response is absent when the hydrogen is placed into the large cages (Figure 2b). Considering that the guest – host cage wall interactions in both cages are of the same nature, it must be the effect of the confinement dimensions that gives rise to this additional dynamic feature.

To verify whether the translational motion of hydrogen molecules inside the cages contributes to the observed excess of density of states (DOS), we performed a series of molecular dynamic simulations. For these simulations we used the Materials Studio and VASP programme suites. The Materials Studio Discover programme was used to perform classical molecular dynamics simulations on hydrogen inside clathrate hydrate stabilised with tetrahydrofuran, using Compass force-field and Ewald summation for both Van der Waals and Coulomb interactions. We simulated the behaviour of 8 unit cells for times of up to 1 ns at various temperatures, using a time-step of 1 fs. VASP was used for ab-initio quantum-mechanical molecular dynamics, where only one primitive cell of the clathrate on the Dirac cluster was simulated at various temperatures and with different hydrogen loadings, for 4 ps using a time-step of 1 fs. Using the nMoldyn programme suite, the dynamic structure factor $S(Q,\omega)$ has been calculated from Materials Studio and VASP trajectories and compared directly with our experimental results.

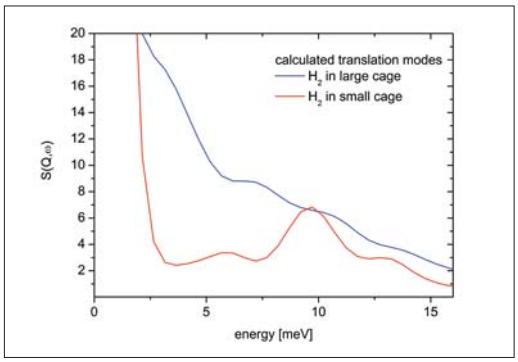

Fig. 3: Dynamic structure factor calculated by WASP software package for translation motion in hydrogen confined in clathrate cages.

The results of molecular dynamics studies are shown in Figure 3. The calculated $S(Q,\omega)$ shows that in the small cage a translation motion (rattling) in the 8-12 meV energy range occurs. The rattling modes shift to low frequencies and become less pronounced when the dimensions of the cage are increased. These are the exact tendencies that we observed in our experiments. It should be noted that the available molecular dynamics tools cannot demonstrate the internal dynamics of the hydrogen molecule, including the rotational motion.

However, the translational motion alone cannot explain the difference between the intensities observed in the small and large cages. Considering the amount of hydrogen in the cages and the numbers of cages in the structure, the intensity of the rattling modes should be about the same in both cages. The excess of DOS observed for hydrogen in the small cages must have an additional dynamic origin. At these temperatures and beyond the translational motion, only the molecular rotation is excited and can contribute to the $S(Q,\omega)$. The energies of rotational and translation dynamics are fairly similar and the coupling between these two modes can lead to a new, hybrid type motion. On the one hand, this can explain the observed excess DOS. On the other hand, the onset of the hybrid motion reflects strong coupling between modes and thus is expected to decrease the kinetic energy of the confined molecular hydrogen. This in turn increases its effective “attachment” to the framework (cage walls) and thus increases the temperature-pressure stability of the entire H_2 clathrate system.

[1] W.Mao, Science 297 (2002) p. 2247
[2] H. Lee et al., Nature 434, 743 (2005)
[3] J.U.Young and J.A. Koppel, Phys. Rev.135A,603 (1964)

Corresponding author:
Margarita Russina
margarita.russina@helmholtz-berlin.de

Does a chiral spin liquid skyrmion phase exist?

C. Pappas[1], E. Lelièvre-Berna[2], P. Falus[2], P. Fouquet[2], B. Farago[2], P. Bentley[1,2], E. Moskvin[1,3] and S. Grigoriev[3]
■ 1 Helmholtz-Zentrum Berlin für Materialien und Energie, Berlin, Germany
■ 2 Institut Laue-Langevin, 6 rue Jules Horowitz, 38042 Grenoble, France
■ 3 PNPI, 188300 Gatchina, Leningrad District, Russia

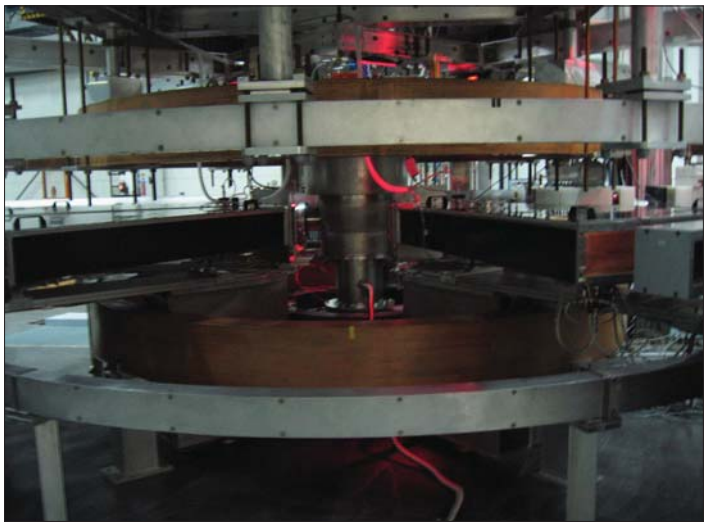

Fig. 1: Photograph of the first realisation of a polarimetric NSE set-up, a combination of Cryopad (at the centre) with the Neutron Spin Echo spectrometer SPAN.

Chirality is ubiquitous in nature and on the microscopic level is of fundamental importance in our everyday life. It is also an essential ingredient for the appearance of countable soliton-like quasi-particles in continuous fields, which bridge the gap between waves and particles in the wave-particle duality concept. These were introduced in the early 1960s by Skyrme [1] and have, until now, been identified in semiconductors under high magnetic fields or in the blue phases of liquid crystals. Chiral interactions may also lead to a spontaneous formation of skyrmions, even in perfect ferromagnetic crystals without any structural defects or external magnetic fields [2]. The condition for the emergence of this novel ground state of condensed matter is a hierarchy of energy scales in the Hamiltonian, which is realised with the reference itinerant-electron ferromagnet MnSi. In MnSi the strongest exchange interaction aligns the spins ferromagnetically and the weaker chiral Dzyaloshinskii-Moriya $(\vec{M} \times (\vec{\nabla} \times \vec{M}))$ term twists the spins into a helix, due to the lack of inversion symmetry of the B20 ($P\,2_13$) lattice structure. Additionally, the weakest Anisotropic Exchange (AE) or crystal field term pins the helix propagation vector $\vec{\tau}$ long the <111> crystallographic directions. The helical order appears below the weak first order transition at $T_C \sim 29$ K with a single-domain, left-handed helix of period ~175 Å ($|\vec{\tau}| \sim 0.036$ Å^{-1}) and all magnetic moments perpendicular to the helix propagation vector.

The rigorous analysis of chirality and chiral fluctuations at the helical transition has required the development of the new technique: polarimetric Neutron Spin Echo spectroscopy, which combines the high energy resolution of Neutron Spin Echo (NSE) with the polarisation analysis capabilities of Cryopad. NSE uses the Larmor precession of polarised neutrons in a magnetic field to directly access the energy transfer at the sample and reaches the highest energy resolution in neutron spectroscopy (< 1 neV). The neutron beam polarisation may be seen as a classical vector in the laboratory but only the component along a quantisation axis (magnetic field) can be measured. A rotation by $\pi/2$, as may occur due to the chiral term in MnSi, will not be distinguished from a depolarisation unless the quantisation axis is not defined at the sample. These Spherical Neutron Polarimetry (SNP) or simply polarimetric measurements are enabled by Cryopad, which shields the magnetic field down to ~0.1 μT and controls the incoming and scattered beam polarisation vectors at the borders of the zero field area, with an accuracy greater than 0.5 degrees.

The Polarimetric NSE method was developed at SPAN (Hahn-Meitner-Institut) (Figure 1) and then implemented at IN15 (Institut Laue-Langevin). The first order helical transition of MnSi is seen by the jump of neutron intensity at the <111> helical reflection (Figure 2a) and corresponds to the sharp peak of the specific heat found by Stishov et al. [5]. These specific heat results are reproduced in Figure 2c. The SNP measurements were performed with an incident beam polarisation as high as 97 % K (Figure 2b) and confirm the stabilisation of a single-domain, left-handed helix at low temperatures. However, this is unaffected by the first order transition and remains unchanged up to $T_{C'} \sim T_C$+1.2 K, the temperature of a broad specific heat maximum. Figure 2 illustrates the existence of two transitions in MnSi.

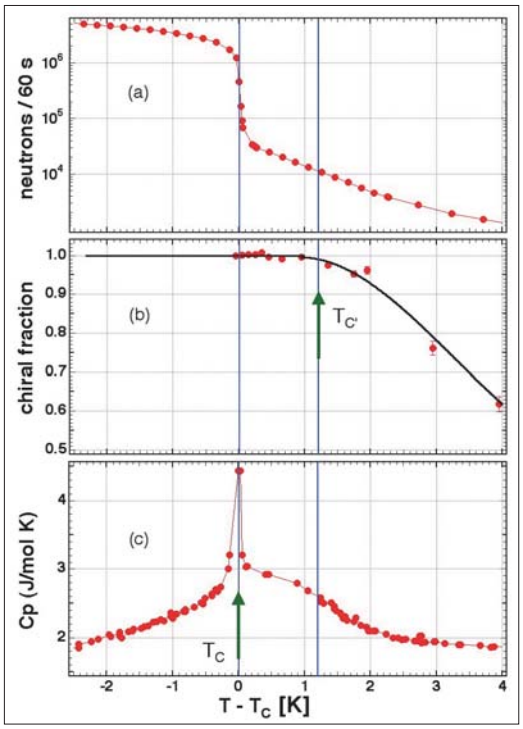

Fig. 2: Temperature dependence of (a) the intensity of the helical peak and (b) the chiral ratio of the dominant left-handed domain. In (b) the red circles are calculated from the extinction of the chiral intensity when the polarisation vector is parallel to the helix propagation vector and the blue squares are deduced from the $\pi/2$ rotation of the polarisation vector (incident vector perpendicular to the helix propagation vector). The specific heat results of Stishov et al. [5] are given in (c). For the sake of comparison the data are plotted against $T\text{-}T_C$, where T_C is determined by the jump in neutron intensity and the peak of the specific heat respectively.

The first order transition to a long range order is seen on the helical peak intensity and the peak due to the specific heat is seen at T_C. The spin liquid state above the helical phase is completely single-handed without any sign of disorder. It is an amorphous skyrmion phase, which exists between T_C and $T_{C'}$ and has strong similarities with nematic liquid crystals.

The dynamic or static nature of this new phase was unravelled by Neutron Spin Echo spectroscopy. The spectra in Figure 3 show exponential relaxations superimposed on an elastic contribution due to the Bragg peak, which were 'fitted' using the function $I(q,t) = a\ \exp(-t/\tau_o) + (1-a)$. The characteristic time τ_o does not change with temperature but the elastic fraction $(1-a)$ evolves from ~20% to 100% within 0.2 K and is very similar to the rapid increase in the intensity seen in Figure 1a and masking the decay of $I(Q,t)$ at T_C.

The amorphous skyrmion phase is completely dynamic and the fluctuations coexist with the helical long range order at T_C. An extensive analysis of the relaxation seen by NSE excludes any interaction between fluctuations and the first order helical transition. Also, high resolution Larmor diffraction experiments do not show any structural deformation at the helical transition [6]. Therefore, the first order transition must be attributed to the different textures between the skyrmion and the helical phases. It is remarkable that chirality, specific heat and the NSE spectra give consistent results. This evidences the existence of this completely chiral single domain but dynamically disordered novel state of matter, which appears in a very narrow temperature range of ~1.2 K above the helical phase of MnSi.

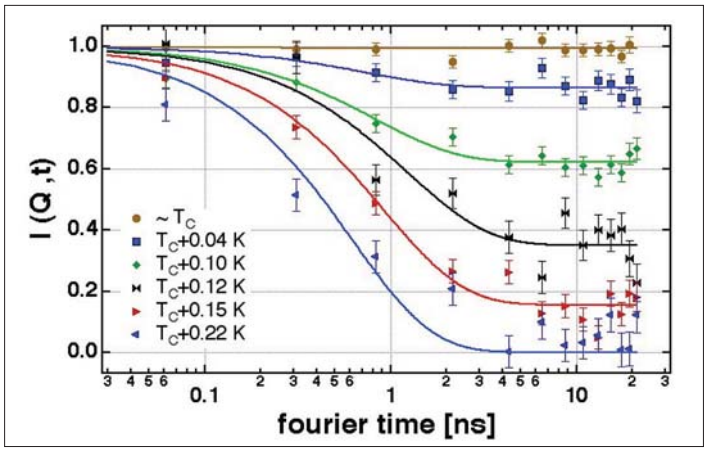

Fig. 3: Polarimetric NSE spectra measured on IN15 with a wavelength of 9 Å for the incoming polarisation vector $\vec{P}'$ perpendicular to the helix propagation vector $\vec{\tau}$ and to the scattering vector $\vec{Q}$. In this case the helix rotates the polarisation by $\pi/2$ and the scattered polarisation vector $\vec{P}$ is parallel to $\vec{\tau}$ and $\vec{Q}$. Such a measurement is only possible in polarimetric NSE configuration.

[1] T.H. Skyrme, Proc. R. Soc. Lond. Ser. A, 260 (1961) 127
[2] U. K. Rößler, A.N. Bogdanov and C. Pfleiderer, Nature 442 (2006) 797
[3] C. Pfleiderer, D. Reznik, L. Pintschovius, H. von Lohneysen, M. Garst, and A. Rosch, Nature 427 (2004) 227
[4] S. V. Grigoriev et al, Phys. Rev. B 72 (2005) 134420
[5] S. M. Stishov et al., Phys. Rev. B 76 (2007) 052405 and S. M. Stishov et al., J. Phys.: Condens. Matter 20 (2008) 235222
[6] C. Pfleiderer, P. Böni, T. Keller, U. K. Rößler, and A. Rosch, Science 316, 1871 (2007).

Corresponding author:
C. Pappas
pappas@helmholtz-berlin.de

Fractional magnetisation plateaus in the Shastry Sutherland magnet TmB_4

K. Siemensmeyer[1], E. Wulf1, H.-J. Mikeska[2], K. Flachbart[3], S. Gabani[3], S. Matas[3], P. Priputen[3], E. Efidokimova[4], N. Shitsevalova[4]

■ 1 Helmholtz-Zentrum Berlin, Glienicker Str. 100, D 14109 Berlin ■ 2 Institut für theoretische Physik, Universität Hannover, D 30167 Hannover ■ 3 Institute of Experimental Physics, Slovak Academy of Science, SK 04001 Kosice, Slovakia ■ 4 Institute for Problems of Material Science, Ukraine Academy of Science, UA 03680 Kiev, Ukraine

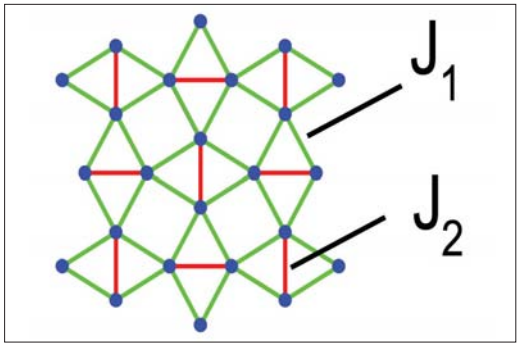

Fig. 1: The position of rare earth ions in the tetragonal plane. The diagonal bonds (red) and the square bonds (green) are almost identical in length, leading to an almost identical exchange path J_1 and J_2.

For decades, the magnetism on geometrically frustrated lattices has fascinated scientists, and numerous, initially exotic and now familiar phenomena have been found. For example, the magnetic order on the triangular and Kagóme lattice in two dimensions (2D), and more recently, the well known pyrochlore structure in 3D, where frustration leads to ferromagnetism and to the emergence of topological magnetic monopoles. Less familiar is a 2D lattice first suggested by Shastry and Sutherland (SS) [1]. It is a square lattice where interactions along the sides of the square and through every second square diagonal are assumed (Figure 1). Interestingly, SS could show that for antiferromagnetic (af) interactions on the sides and dominant af interaction on the diagonals, an af spin dimer is formed that condenses into a dimer spin liquid state.

Reports on this lattice are scarce. To date, the compound $SrCu(BO_3)_2$ has produced most of the knowledge on the properties of such a lattice. Most surprising is the observation of fractional magnetisation plateaus in $SrCu(BO_3)_2$, which was not predicted by the theory [2,3]. The specific explanations for this observation are still subject to debate, presumably because the critical fields for

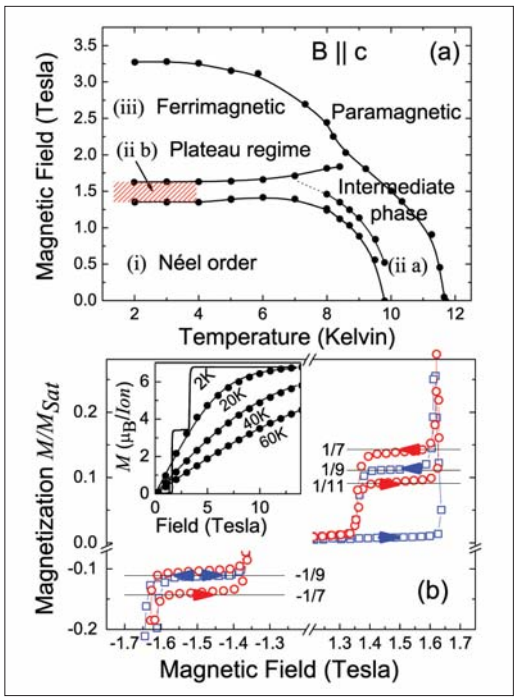

Fig. 2: (a) Phase diagram of TmB_4 as derived from magnetisation data for B || (001) (full symbols). (b) Magnetisation at T = 2K (open squares) and T = 3K (open circles). The arrows indicate the direction of the field change. The inset in (b) gives an overview of high field; the lines are measured data and full circles are calculated using a high temperature approximation.

$SrCu(BO_3)_2$ are beyond those available for scattering experiments and are focused on an analogy with the fractional quantum Hall effect of a 2D fermion gas [4].

Recently, we have investigated another class of SS magnets formed by a series of rare earth tetraborides – REB_4 [5]. The geometry of the REB_4 lattice can be mapped to a SS lattice. In general, the magnetisation data show that these materials are highly anisotropic magnetic metals. Out of a series of compounds investigated by us (RE=Tb, Er, Ho, Tm), it transpired that TmB_4 shows fractional

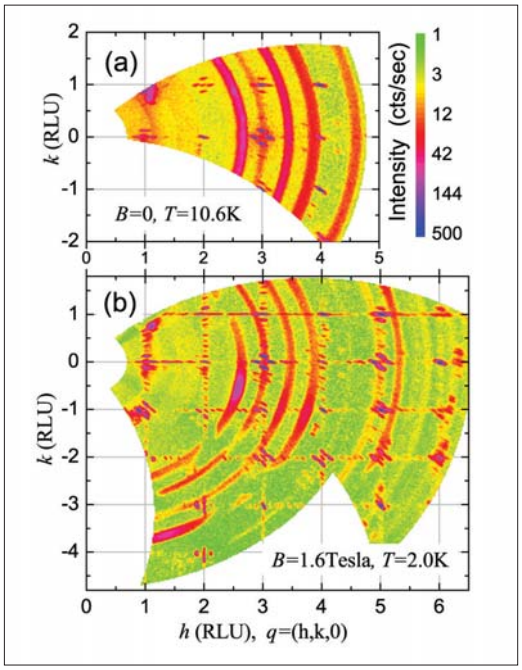

Fig. 3: (a) and (b) show the neutron diffraction pattern in the tetragonal plane for the intermediate and the plateau phase respectively. The figures share the intensity colour code given in (a). The reflections can be indexed based on fractions of 1/7, 2/7… and 1/9, 2/9… . The powder lines are generated by the aluminium of the cryogenic equipment used for the neutron diffraction experiments.

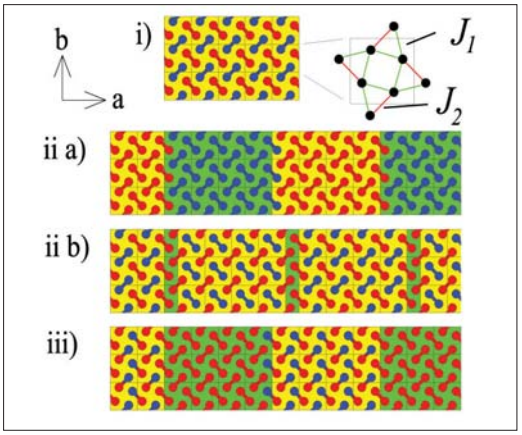

Fig. 4: The magnetic structure of TmB_4 for a magnetic domain along the a⁻ direction in the tetragonal plane. Red or blue circles denote up or down Ising moments. The labels (i) to (iii) refer to the phase identification in Figure 2(a). In (i) the position of the Tm_{3+} ions within the tetragonal plane is expanded for one unit cell, with the SS-bonds marked in red.

magnetisation plateaus as a function of the external field at values of M/M_{sat}= *1/7, 1/8, 1/9, 1/11…* . It shows af order and is dominated by a strong Ising anisotropy. The phase diagram (Figure 2) reveals four different regimes. A low temperature zero field phase is separated from the paramagnetic phase by another af ordered phase. In high field the order is ferrimagnetic with M/M_{sat} = ½. The zero field phase and the ferrimagnetic phase are separated by a regime where fractional magnetisation values are observed at low temperature.

The critical temperatures and magnetic fields of TmB_4 are experimentally easy to access, in contrast to the $SrCu(BO_3)_2$. This provided the first opportunity to study the magnetic structures on an SS - lattice using neutron diffraction (Figure 3). In the zero field low temperature phase, the moments of the dimer pairs are ferromagnetically (fm) aligned, though the coupling between dimers is af (c.f. Figure 4). The high temperature, zero field phase shows regions with fm dimer coupling, and the direction of the fm alignment alternates on a length scale of 8 unit cells. The fractional states form similar structures where stripes of fm phase slips – like domain walls – are added. They lead to the observed fractional magnetisation. Finally, the ferrimagnetic phase consists of stripes of fm and af dimer order with a periodicity of 8 unit cells. Interestingly, in the "af" stripe, the magnetic moments of a dimer pair are af.

Our data could possibly be explained by the RKKY interaction that is believed to be the dominant interaction in metallic REB_4 compounds. This, however, is not satisfactory because more specific interaction ratios are required to explain the structures in the various phases, in particular in the fractional regime. For the similar compound $SrCu(BO_3)_2$, a Hofstadter treatment [6] analogous to the fractional quantum Hall effect has been proposed [4] and this provides a much more natural approach to explain the magnetism in TmB_4. Consequently, we speculate that TmB_4 is a magnetic analogue to a spinless 2D fermion gas in a strong field. In that material class TmB_4 would be the first example that is fully accessible to experimental studies.

[1] B. S. Shastry and B. Sutherland, Physica 108B, 1069 (1981).
[2] H. Kageyama et al., Phys. Rev. Lett. 82, 3168 (1999).
[3] K. Kodama et al., Science 298, 395 (2002).
[4] S. E. Sebastian et al., e-print Phys. Rev. Lett. 101, 177201 (2008)
[5] K. Siemensmeyer et al., Phys. Rev. Lett. (2008).
[6] D. R. Hofstadter, Phys. Rev. B 14, 2239 (1976).

Corresponding author:
Konrad Siemensmeyer
siemensmeyer@helmholtz-berlin.de

From the bronze to the iron age of superconductivity

D.N. Argyriou*, S.A.J. Kimber*, Karel Prokes and Fabiano Yokaichiya*
■ Helmholtz-Zentrum Berlin für Materialen und Energie, *Novel Materials Group, Department SF-2.

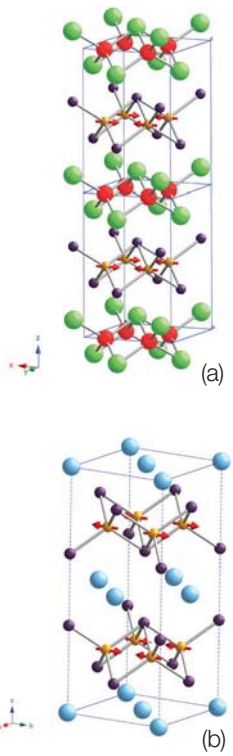

1986 was a seminal year in physics. Karl Müller and Johannes Bednorz in their lab in Zurich discovered that a particular copper oxide showed superconductivity at T_C=35 K, a temperature that was almost 12 K higher than any other known superconductor at the time[1] . This discovery indicated that superconducting T_Cs can be pushed from a few Kelvin to an unprecedented 140 K. Although there is still much debate on the exact mechanism that drives superconductivity in copper oxides, what is increasingly clear is that the magnetic moment of the copper ions provides a major component of the glue between electrons that forms Cooper pairs and produces superconductivity. So, if copper with its magnetic interactions is good for superconductivity, then why not other magnetic transition metals, too, such as Fe, Co, Ni or Mn? Recently, there was a discovery in hydrated $NaCoO_2$ compounds that yielded superconductivity with a relatively low T_c of 5 K[2]. However, interest in this material was brushed aside at the beginning of 2008 by the discovery that compounds that have iron arsenide layers show superconductivity as high as 55 K[3] (see Fig. 1). The field has developed very rapidly since then, with the discovery of a host of layered materials that have FeAs, FeSe and NiP layers that show superconductivity, and all in the space of a few months!

Fig. 1: Crystal structures of the FeAs superconductors. In this type of superconducting materials the FeAs layer is made of edge shared $FeAs_4$ tetrahedra, that are separated either by a REO (rare earth) layer as in the case of the so-called "1111" family (a) or a divalent cation as in the case of the "122" family (b).

Why so much interest in a 55 K superconductor? Firstly, superconductivity in these iron arsenide compounds is more isotropic (in-plane versus out-of-plane) than the copper oxides which are notorious for their high anisotropy and the technological problems it presents. Therefore, the high T_C and lower anisotropy of the iron arsenides open up huge potential for technological applications. Secondly, magnetism may also be important for achieving superconductivity as the iron arsenides form another class of materials that allow the investigation of magnetically-mediated Cooper pairing. It turns out that on the one hand, there are great similarities to the behaviour of copper oxides, while on the other, there are dramatic differences. Like the copper oxides, the (undoped) parent compounds are also antiferromagnets, and chemical doping with hole charges suppresses long range magnetic order and yields superconductivity. Unlike the undoped magnetic copper oxides that are Mott insulators, the iron arsenides are metals in their undoped magnetic state. Another marked difference that has changed the way we think about superconductivity in these materials, is that applying pressure on the magnetic parent compound itself yields superconductivity at almost the same value of T_C as we obtain by chemical doping. This effect has never been observed in the copper oxides. The effect of pressure is most pronounced in the 122 family of compounds AFe_2As_2 (see Fig. 1), where T_C for A=Ca is 12 K at 5 kbar and up to 38K at 50 kbar for A=Ba.

At HZB we have investigated the development of magnetism in iron arsenide parent compounds and the effects of pressure on the crystal and magnetic structure in close collaboration with the Leibniz-Institut für Festkörper- und Werkstoffforschung, Dresden, and the Ames Lab. in the USA. We first looked at PrFeAsO. The structure of this compound consists of layers of PrO and FeAs as shown in Fig.1. Using neutron powder diffraction we showed that both the Fe and the Pr spins order long range and beyond this, a magnetic coupling between these two atoms leads to an unusual negative thermal expansion along the *c*-axis on cooling[4]. The magnetic structure we established for Fe is also shown in Fig.1 and confirms much of the initial calculation of magnetic order[5].

Our work with pressure has focused on the 122 family of compounds aided by small single crystals. Here we found that as we apply pressure on $CaFe_2As_2$ and the material becomes a superconductor above 3 kbar[6], at the same time the crystalline lattice collapses in volume by 5%, while all evidence of ordered magnetism disappears from the neutron diffraction data[7]. This exciting result suggests that the changes to the lattice are intimately linked to the changes in magnetic and electronic degrees of freedom. At ambient pressure we established that the high temperature tetragonal phase (T) discontinuously changes to an orthorhombic phase (O) exactly at the magnetic transition[8]. The ordering of Fe-spins in 122 is the same as in the 1111 type of compounds (see Fig. 1). Us-

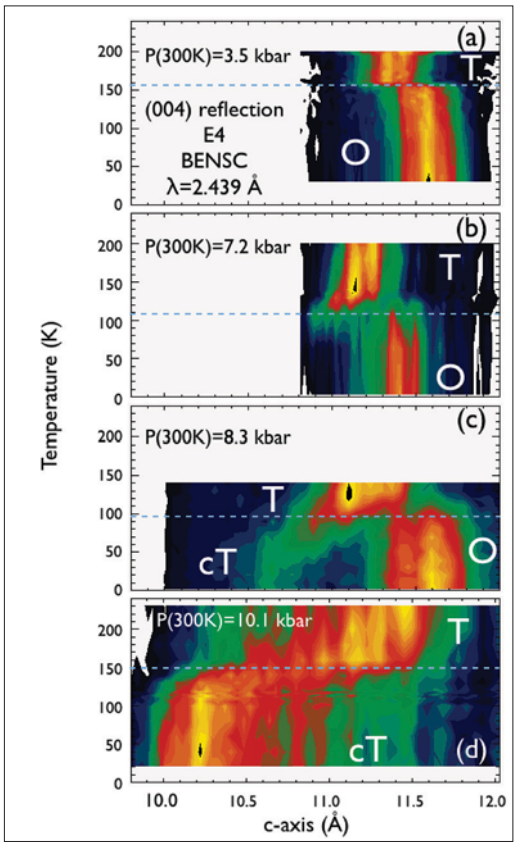

Fig. 2: Temperature dependent neutron diffraction measurements at various initial pressures, collected on the E4 diffractometer from a 10 mg $CaFe_2As_2$ single crystal inside a clamped pressure cell. Here we show measurements of the (004) reflection. The data are represented as two dimensional colour plots with intensity shown as colour.

ing the double axis diffractometer E4 at BENSC we were able to follow the structural and magnetic transitions as a function of pressure and temperature as our $CaFe_2As_2$ single crystal was driven into the superconducting state. In Fig. 2, we show the (004) reflection as a function of temperature measured in a clamped pressure cell on E4. Here, on cooling, the pressure changes by ~2 kbar from 300 to 2K from the initial pressure set ex situ (P(300K)). At low pressures we observe the same T-O transition as we find at ambient pressure indicated by a small discontinuous expansion of the c-axis (Fig. 2(a-b)). However, at high pressure we can observe the new collapsed tetragonal (cT) phase that hosts superconductivity. Here the *c*-axis shrinks abruptly by 1Å, a change of almost 10% in the c-axis (Fig. 2(d)). But with intermediate pressure we find evidence of co-existence between the O and cT phases (Fig. 2(c)) that may help explain observations of co-existence between magnetism and superconductivity. Using the same measurements and others with our collaborators we also probed the magnetic order and found that it abruptly disappears as we enter the cT phase. Our results show that the effect of chemical doping on long range magnetism resembles that of pressure.

Our results firmly establish the iron arsenides as a different class of superconductors from copper oxides, despite their similarities. In this new iron age of superconductivity we have more than one way of tuning the lattice to produce superconductivity: chemical doping and pressure. This flexibility allows us to probe the changes in the electronic and crystal structure cleanly with pressure and without the local distortions that unavoidably develop when using chemical doping. Even if it turns out that magnetic fluctuations aid Cooper pairing to produce superconductivity, the way these fluctuations are tuned to optimum values in the iron arsenides is quite different from that in copper oxides. It is still the dawn of this new iron age in superconductivity and there is much more to learn. What is certain is that the results obtained so far are unexpected and exciting and promise to keep us busy for years to come.

[1] J. G. Bednorz and K. A. Müller Z. Physik, B 64, 189 (1986).
[2] K. Takada, et al. Nature 422, 53 (2003).
[3] Y. Kamihara, T. Watanabe, M. Hirano, and H. Hosono. J Am Chem Soc 130, 3296 (2008); Ren Zhi-An, LU Wei, Yang Jie, Yi Wei, Shen Xiao-Li, Li Zheng-Cai, Che Guang-Can, Dong Xiao-Li, Sun Li-Ling, Zhou Fang, Zhao Zhong-Xian. Chinese Phys Lett 25, 2215 (2008).
[4] S.A.J. Kimber, D. N. Argyriou, F. Yokaichiya, K. Habicht, S. Gerischer, T. Hansen, T. Chatterji, R. Klingeler, C. Hess, G. Behr, A. Kondrat, and B. Büchner. Phys. Rev. B 78, 140503 (2008).
[5] T. Yildirim, Phys Rev Lett 101, 057010 (2008).
[6] M. Torikachvili, Sergey L. Bud'ko, Ni Ni, and Paul C. Canfield. Phys Rev Lett 101, 057006 (2008).
[7] A. Kreyssig, M. A. Green, Y. Lee, G. D. Samolyuk, P. Zajdel, J. W. Lynn, S. L. Bud'ko, M. S. Torikachvili, N. Ni, S. Nandi, J. Leão, S. J. Poulton, D. N. Argyriou, B. N. Harmon, P. C. Canfield, R. J. McQueeney and A. I. Goldman. Phys Rev B (in press). arXiv:0807.3032.
[8] A. I. Goldman, D. N. Argyriou, B. Ouladdiaf, T. Chatterji, A. Kreyssig, S. Nandi, N. Ni, S. L. Bud'ko, P. C. Canfield and R. J. McQueeney. Phys. Rev. B 78, 100506 (2008).

Corresponding author:
Dimitri Argyriou
argyriou@helmholtz-berlin.de

Antiferromagnetic order in thin films with atomic layer resolution

E. Schierle[1,2], A. Gottberg[2], W. Söllinger[3], W. Heiss[3], G. Springholz[3], G. Kaindl[2] and E. Weschke[1,2]

■ 1 Helmholtz-Zentrum Berlin für Materialien und Energie, Berlin, Germany ■ 2 Institute of Experimental Physics, Freie Universität Berlin, Berlin, Germany ■ 3 Institute of Semiconductor Physics, Johannes Kepler Universität, Linz, Austria

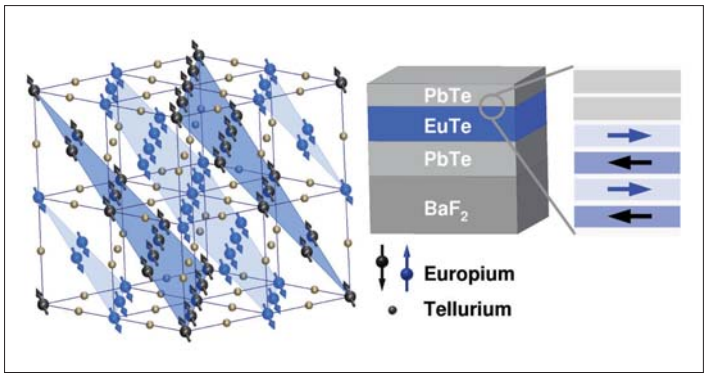

Fig. 1: Magnetic structure of EuTe with antiferromagnetic stacking of ferromagnetic (111) planes along the diagonal of the cubic crystal structure. Thin film samples are grown on PbTe buffer layers on BaF_2 substrates with the [111] direction perpendicular to the film surface.

In the vicinity of surfaces and interfaces, magnetic order and its thermal evolution may deviate from bulk behaviour [1]. A well-known example employed in current magnetic thin film devices is the exchange bias effect, where the hysteresis loop of a ferromagnet is shifted in the presence of the interface to an antiferromagnet. The understanding of such phenomena requires a detailed knowledge of the local magnetic structure, particularly as a function of the distance from the interface. While scanning probe techniques can readily provide lateral magnetic images on an atomic scale, a depth-dependent characterisation of magnetic structures with the same resolution remains a challenging task. Nuclear techniques are well suited to studying local magnetic properties but require the insertion of probe isotopes into the material. Magnetic scattering techniques are also applicable; however, they usually suffer from the weakness of the signal that is obtained from the few atomic layers of a thin film.

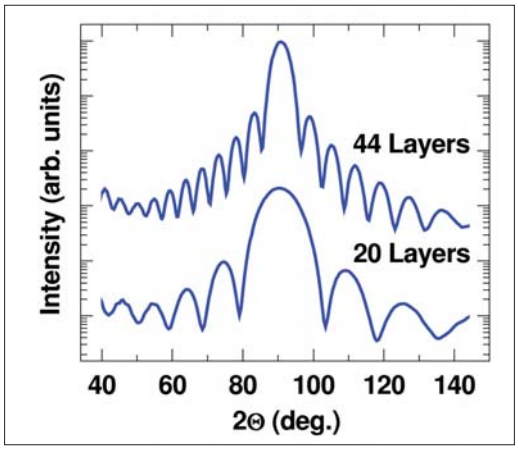

Fig. 2: The (½ ½ ½) magnetic Bragg peak obtained from EuTe films by resonant magnetic soft x-ray diffraction. The smaller number of scattering layers of the thinner film is observed in the diffraction patterns as a broadening of the main peak and shifts of the side maxima.

With the advent of third-generation synchrotron radiation sources, a magnetic x-ray scattering technique has become available. By tuning the photon energy to a core-electron excitation, resonance can increase the magnetic x-ray scattering length substantially. The effect is huge at the $M_{4,5}$ edges of the lanthanide elements, and the magnetic x-ray scattering by a single lanthanide ion can be as large as conventional charge scattering from 200 electrons [2]. The $M_{4,5}$ edges cover the soft x-ray range between 900 eV and 1500 eV. These photon energies are provided by the UE46 beamline of Helmholtz-Zentrum Berlin at BESSY II [3], an instrument that is ideally suited for this type of studies.

In the present investigation, the atomic-layer resolved magnetisation profile of an antiferromagnetic thin film was obtained for the first time [4]. This was achieved with a thin film of the magnetic semiconductor europium telluride (EuTe), which allowed exploitation of the high sensitivity at the M5 resonance. EuTe is a prototype Heisenberg system that was studied extensively as bulk material. It crystallises in the cubic rock salt structure (Figure 1). The (111) planes are ferromagnetically ordered, with antiferromagnetic stacking along the [111] direction. Along this direction, the magnetic unit cell is twice as large as the chemical unit cell, and a (½ ½ ½) magnetic Bragg peak is

observed. Single EuTe (111) films, sandwiched between lead telluride (PbTe), were prepared with very high crystalline quality by molecular beam epitaxy [5]. With the photon energy tuned to the Eu-M_5 resonance (1127.5 eV), the magnetic (½ ½ ½) reflection could be recorded with unprecedented quality: peak count rates were larger than 10^8 photons/sec with signal-to-background ratios of more than 1000. This allowed a detailed study of peak shapes and intensities as a function of temperature even close to the ordering temperature of 12.8 K.

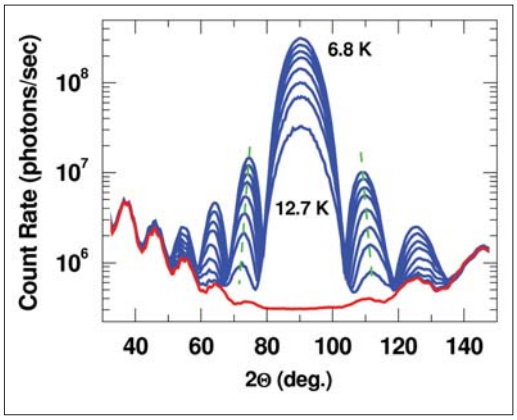

Fig. 3: Magnetic diffraction patterns obtained from the 20-layer film at various temperatures. Note the shift of the side maxima due to a decreasing mean number of magnetic layers with increasing temperature.

The sensitivity of the magnetic diffraction patterns is illustrated in Figure 2. With a finite number of scattering planes, the diffraction pattern of a 44-layer thick film exhibits pronounced side maxima, known as Laue oscillations. For 20 layers, the pattern is strongly broadened with side maxima shifted away from the main peak. An analogous result is well known from basic wave optics: the width of the diffraction signal of a slit is inversely proportional to its width (corresponding to the film thickness in our case). The same phenomenon, albeit in a more subtle manner is observed for the 20 layer film upon increasing the temperature (Figure 3): the shift of the side maxima indicates a reduction of the mean number of magnetically ordered layers as the ordering temperature is approached. By using a large number of data sets for various temperatures, this can be worked out in more detail by a rigorous simultaneous analysis. As a result, the magnetisation of each individual layer of the film is obtained as a function of temperature (Figure 4). At the lowest temperature, a rather sharp profile is observed, essentially all layers are fully magnetised. With

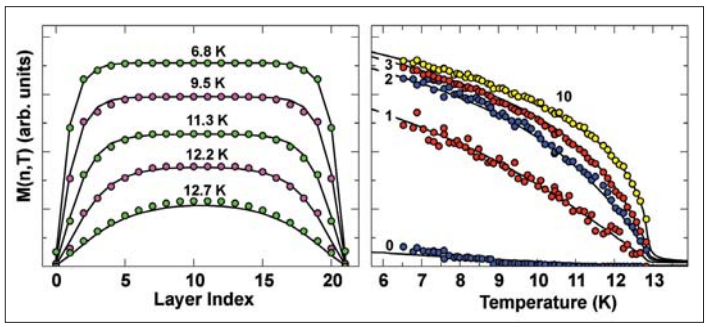

Fig. 4: Layer-resolved magnetisation in a EuTe film of 20 atomic layers as obtained from resonant magnetic soft x-ray diffraction. Left: Magnetisation profiles for various temperatures. In the layers close to the interfaces, the magnetisation is strongly reduced. Right: Temperature dependences of selected layers. The inner layer (10) behaves in a bulk like manner, while strong deviations are observed for the outer layers (0-3) as theoretically predicted [1]. The solid lines represent the result of Monte-Carlo calculations [4].

increasing temperature, the profiles become increasingly rounded, which is due to the reduced exchange energy at the EuTe/PbTe interfaces that leads to a faster decrease in the magnetisation in this region. Consequently, the temperature dependence of the magnetisation exhibits a clear variation across the film. The behaviour of the inner layer is comparable to that of bulk EuTe, while strong deviations are observed for layers in the vicinity of the interface.

These results not only corroborate theoretical predictions experimentally [1], but also pave the way for diffraction studies of magnetic ordering at surfaces and interfaces with very high depth resolution. Furthermore, the method is applicable to more subtle ordering phenomena, such as charge and orbital ordering that can be seen in transition metal oxides by resonant x-ray diffraction [6].

[1] K. Binder and P. C. Hohenberg, Phys. Rev. B 9, 2194 (1974).
[2] H. Ott et al., Phys. Rev. B 74, 094412 (2006).
[3] U. Englisch et al., Nucl. Instr. and Meth. Phys. Res. A 467- 468, Part 1, 541 (2001).
[4] E. Schierle et al., Phys. Rev. Lett. (almost accepted).
[5] N. Frank, G. Springholz, and G. Bauer, Phys. Rev. Lett. 73, 2236 (1994).
[6] P. Abbamonte et al., Nature 431, 1078 (2004).

Corresponding author:
E. Schierle
enrico.schierle@helmholtz-berlin.de

Spin-polarized neutron imaging

Nikolay Kardjilov, Ingo Manke, Markus Strobl, André Hilger, Martin Dawson, John Banhart
■ **Helmholtz-Zentrum Berlin für Materialien und Energie, Berlin, Germany**

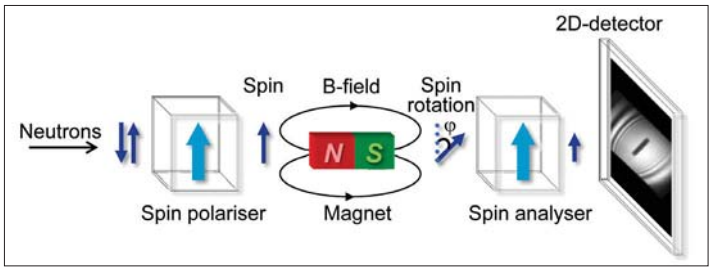

Fig. 1: Schematic diagram of the set-up used for imaging magnetic materials on CONRAD. The neutron beam is polarized, allowed to precess around a magnetic field, analyzed, and then detected. Note how the intensity (dark blue arrow) behind the analyzer is smaller than the intensity behind the polarizer. [1]

Introduction

Conventional approaches for imaging magnetic fields are limited to investigating the surface of a sample and the free space around it; the observation of the spatial distribution of magnetic fields within a bulk sample is not possible. In order to overcome this problem, a new imaging technique has recently been proposed [1,2]. This new method uses neutrons, subatomic particles whose zero net electrical charge allows them to penetrate thick layers of matter, but whose intrinsic magnetic moment makes them highly sensitive to magnetic fields. Utilizing the magnetic interaction of a spin-polarized neutron beam, it is possible to visualize magnetic fields both in free space and in the bulk of solid, massive, opaque samples, revealing the field line distribution both in two and three dimensions [3,4,5].

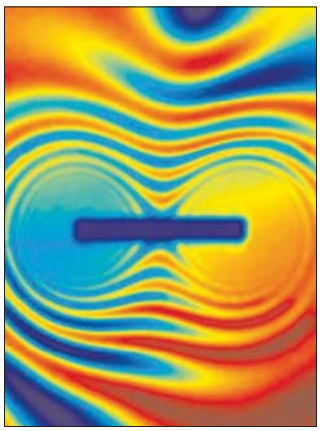

Fig. 2: A radiograph showing the field lines surrounding a bar magnet. The magnetic field decreases in strength with distance from the magnet, resulting in a series of maxima and minima, where the beam polarization is sequentially parallel or anti-parallel, respectively, to the analyzer. Very close to the magnets (where the field is strongest) the field lines are too close together to be resolved spatially [3,4].

Polarized neutron radiography

The neutron is sensitive to magnetic fields due to its magnetic moment, which is anti-parallel to its spin. In the presence of a magnetic field the magnetic moment will undergo a Larmor precession around the field. Polarized neutron radiography is based on the spatially-resolved measurement of the final (cumulated) precession angles of a polarized neutron beam (one in which all spins point in one direction) that traverses the magnetic field of the sample. For monochromatic neutrons (neutrons with a uniform velocity) the precession angle can be related to the average strength of the magnetic field through which the neutrons passed. A polarization analyzer located behind the sample converts this angle to an intensity which is measured by a 2D position sensitive detector. The recorded two-dimensional projection image is then determined by the original intensity modified by a product of the normal absorption contrast and the contrast given by the spin analysis due to the rotation of the polarization vector in the magnetic field [1].

Experiments

Magnetic imaging experiments with polarized neutrons have recently been undertaken on the COld Neutron RADiography and tomography facility (CONRAD) at HZB. The setup used a spin□filter to polarize a neutron beam, which was then allowed to pass through a magnetic sample before being analyzed with a second spin□filter and detected by a position sensitive detector (Figure 1). The key to the image thus formed is that the analyzer only transmits the component of the beam polarization that is parallel to its own polarization axis. As a result, the intensity measured behind the analyzer is the initial beam intensity modulated both by conventional absorption (the magnitude of which can be found from a standard radiograph) and by some sinusoidal function that is directly related to the angle by which the polarization has precessed. The maximum (minimum) intensity will be measured when the beam polarization and the analyzer are aligned perfectly parallel (anti□parallel). This has been demonstrated with a variety of magnetic systems. Figure 2 reveals the familiar pattern of field lines surrounding a simple dipole magnet. The rainbow color scale (from blue = minimum to red = maximum) used in the images is related to the intensity variations induced by the sample and by the presence of a magnetic field [3,4]. The decay of the magnetic field strength with distance is indicated by the annular structure of minima (blue) and maxima (red) representing the periodical 2ϖ rotation of the neutron spin. For the quantification of the magnetic field an iterative calculation algorithm based on Biot-Savart law was developed [1]. The comparison between calculated and measured images for a dipole magnet levitating over a

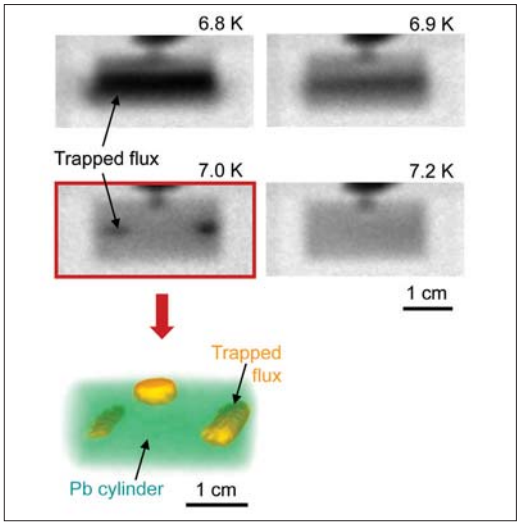

Fig. 4: A three-dimensional reconstruction of trapped flux (yellow regions left and right) inside a polycrystalline cylinder of lead. When cooled to below its critical temperature in the presence of a weak magnetic field, some flux is present inside due to defects and grain boundaries, and this remains trapped even after the field is switched off [1].

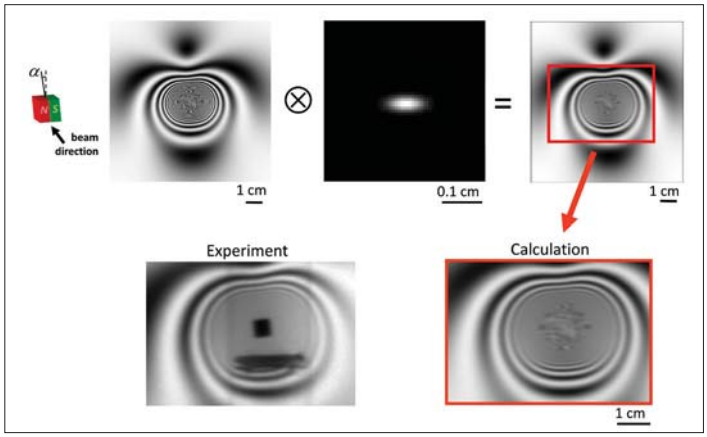

Fig. 3: Comparison of measured and simulated spin polarised neutron radiographies of a dipole levitation over a superconductor: Radiographic image of the levitating dipole (tilted at α=3°) retrieved by a calculation procedure using Biot Savart's law (top) [1]. The corresponding map of the neutron spin rotation in the field was converted into a gray scale image that was convoluted with the resolution function of the instrument. In the central part of the image around the location of the dipole the magnetic field is very strong (up to 1.6 T), causing image artefacts due to the limited sampling of the simulation. Comparison of calculation and experiment (bottom).

superconductor ($YBa_2Cu_3O_7$) is shown in Figure 3. This imaging with spin polarized neutrons can also be extended into three-dimensions using a standard tomographic technique in some instances, as indicated in Figure 4, which shows the distribution of a magnetic field trapped inside a lead cylinder that becomes superconductive when cooled below the critical temperature, $T_c = 7.2$ K [1,2].

Outlook

Spin-polarized neutron imaging is a non-destructive method that provides a number of advantages compared to 2D magnetic imaging techniques using garnet films or scanning techniques (for magnetic fields outside of the sample). The method is applicable to very different environmental set-ups (e.g. for low or high temperature investigations) and samples can be investigated from almost any viewing angle. In this way 3D information about the field distribution can be revealed (even if no mathematical tomographic reconstruction is applied). Measurements are fast because approximately one million pixels are acquired per image within a time-range of several seconds to several minutes. No other method can compete with these advantages even in free space and, as demonstrated, time- and space-resolved measurements become possible.

The presence and controlled application of magnetic fields are essential in many areas of science and technology as well as in fundamental physics. For example, investigations of flux distribution and flux pinning in large superconducting samples [1, 2], the skin effect in conductors [5] or magnetic domain distributions in bulk ferromagnets could be visualized and studied in detail. Finally, the radiographic technique can be extended to tomography in order to investigate and visualize magnetic fields three-dimensionally.

[1] N. Kardjilov, I. Manke, M. Strobl, A. Hilger, W. Treimer, Th. Krist, M. Meißner, J. Banhart, *"Three-dimensional imaging of magnetic fields with polarized neutrons"*, Nature Physics 4, pg. 399-403 (2008)
[2] Nature Physics, press release, www.nature.com/nphys/press_releases/nphys0308.html
[3] I. Manke N. Kardjilov, A. Hilger, J. Banhart, *"Einblicke in Magnetfelder"*, Physik in unserer Zeit 4, July 2008.
[4] N. Kardjilov I. Manke, A. Hilger, M. Dawson, J. Banhart, *"Spin-polarized Neutron Imaging"*, Advanced Materials & Processes, July 2008.
[5] I. Manke, N. Kardjilov, M. Strobl, A. Hilger, J. Banhart, *"Investigation of the skin effect in the bulk of electrical conductors with spin-polarized neutron radiography"*, Journal of Applied Physics 104, 1 (2008).

Corresponding author:
Nikolay Kardjilov
kardjilov@helmholtz-berlin.de

Coating of meso-porous metallic membranes with oriented channel-like fine pores by pulsed laser deposition

N. Wanderka, N. Kardjilov
■ Helmholtz-Zentrum Berlin für Materialien und Energie, Berlin, Germany

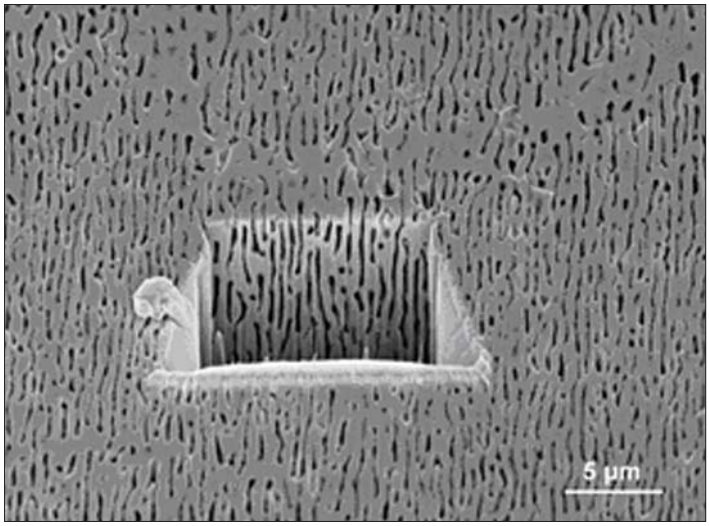

Fig. 1: A slit-type groove, ~10 µm long and of similar width on the membrane surface cut by FIB. Coating on the pore walls was investigated on the cross sections of the porous membrane.

The preparation of thin porous membranes with oriented pore structures has received considerable attention. This is because such structures provide advantages in many applications; for example, separation, catalysis, biosensors, fuel cells/batteries, chemical/microelectronic/photonic devices and therapeutic or diagnostic systems for biotechnology. Such meso-porous metallic membranes can be fabricated (amongst other techniques) by the removal of electrochemical material from simple two-phase metallic alloys. A single-crystal nickel (Ni)-based superalloy (i.e. CMSX4), was used for fabrication of the meso-porous membrane in this study. The alloy was heat-treated to contain a coherent dispersion of Ni_3Al type γ' - precipitates in a γ phase Ni-solid solution matrix. By exploiting the natural tendency of self-assembly of the coherent γ'- precipitates that exists in such alloy systems (due to the anisotropic lattice misfit distribution), the precipitates align and agglomerate into a continuous interconnected network (commonly known as rafting c.f. Fig. 1), when the superalloy is subjected to a thermomechanical treatment. Such a microstructure is suitable for producing the porous membrane.

Coating on a meso-porous substrate is a great challenge and a uniform coating on all pore walls is difficult to produce, especially when the pores are very fine. The pulsed laser deposition (PLD) method was used in this study to coat the porous membrane with two different materials, diamond-like carbon (DLC) and titanium (Ti). DLC and Ti were chosen due to their high compatibility to human tissue and blood cells. It is envisaged that the biocompatibility of the Ni_3Al membrane material may also be improved by the deposition of thin surface layers of DLC or Ti. Such coated membranes may find applications in tissue engineering or in body implants. The aim of the present work was to present the results of the initial experiments with PLD deposition.

Characterisation of coated membranes was carried out in dual-beam system using Carl Zeiss 1540ESB CrossBeam® workstation, which combines an ultra-high resolution GEMINI® field emission column with the high performance focused ion beam (FIB) column. Cross sections of the porous membrane were investigated after cutting a slit-type groove ~10–15 µm long and of similar width on the membrane surface with the ion beam (Fig. 1). In Figure 2, the cross section of the porous membrane coated with DLC is shown. The image actually shows that the membrane surface and the cut cross section are joined at an edge (marked in Figure 2). Whilst the coating on the membrane surface is smooth and hardly distinguishable, the coating on the pore walls is clearly discernible. From this image it is clear that the plasma plume has penetrated all the pores and coated the pore walls. The carbon coating is in the form of a thin continuous film of about 50 nm in thickness. Even for small porous regions (marked with an arrow in Figure 2) there is deposition of carbon. The 3D representation of the porous membrane structure based on the stacking of 178 FIB slice images, after subsequent processing with an algorithm, is shown in Figure 3. The pores have a channel-like formation. A digital

rendering of the 3D volume allows for visualisation of the pore structure by the setting of different levels of opaqueness for the dense material and the hollow spaces. From the inversely rendered image where only the pores are visible, one can see that they are interconnected (Fig. 3(b)).

The PLD process presents a good technique for coating inside pores in the meso-porous membranes up to a thickness of 125 (from one side) and 250 μm (from both sides). The use of FIB for preparing the cross section in the dual-beam system is a useful way to characterise the coatings on the pore walls.

Acknowledgments
FIB/SEM Microscope was purchased with funding from European Union, City State of Berlin and Helmholtz-Zentrum Berlin für Materialien und Energie. This work was performed in cooperation with TU Braunschweig (Dr. D. Mukherji, Prof. J. Rösler) and Laser Center Leoben (J. Lackner), Austria.

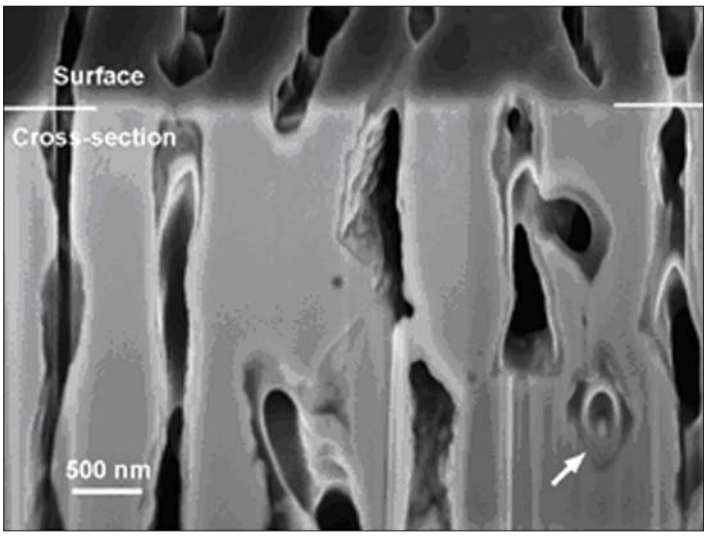

Fig. 2: Cross section of the coated porous membranes. A thin film of carbon coating is clearly discernible on the pore walls. Although the film is continuous, it is not adhering at all places on the pore walls and rather closes and chokes the pores in some channels.

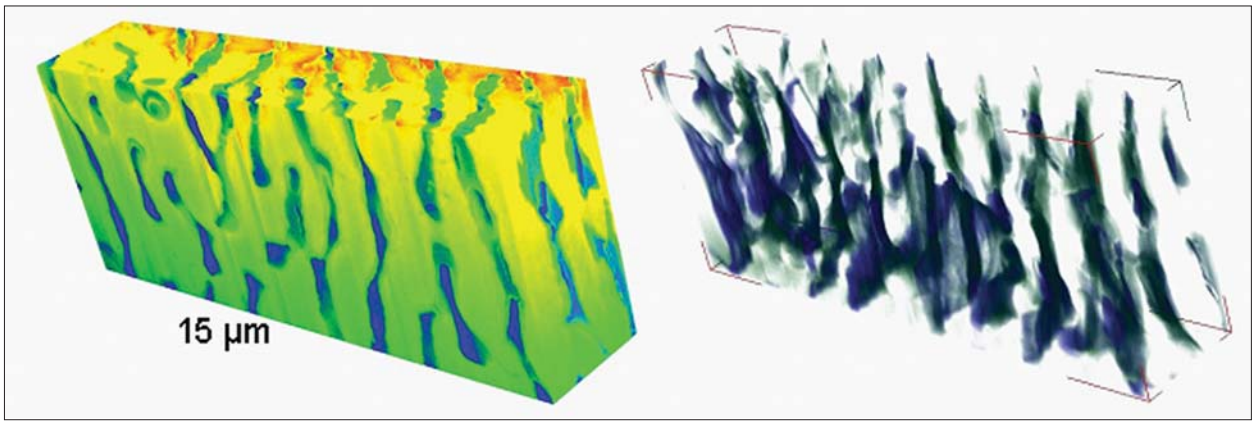

Fig. 3: 3D representation of the porous membrane structure. The volume reconstructed by FIB tomography is approximately 15 μm wide, 7 μm high and 2.5 μm in depth and shows interconnected pores. (a) Reconstructed volume, (b) the inversely rendered image, where only the pores are visible. The pores have a channel-like formation and are interconnected.

Corresponding author:
N. Wanderka
wanderka@helmholtz-berlin.de

Fast radioscopy on liquid metal foams

F. Garcia-Moreno[1,2], A. Rack[3], J. Banhart[1,2]

■ 1 Helmholtz-Zentrum Berlin für Materialien und Energie, Berlin, Germany ■ 2 TU-Berlin: Technische Universität Berlin ■ 3 ESRF: European Synchrotron Radiation Facility, Grenoble, France

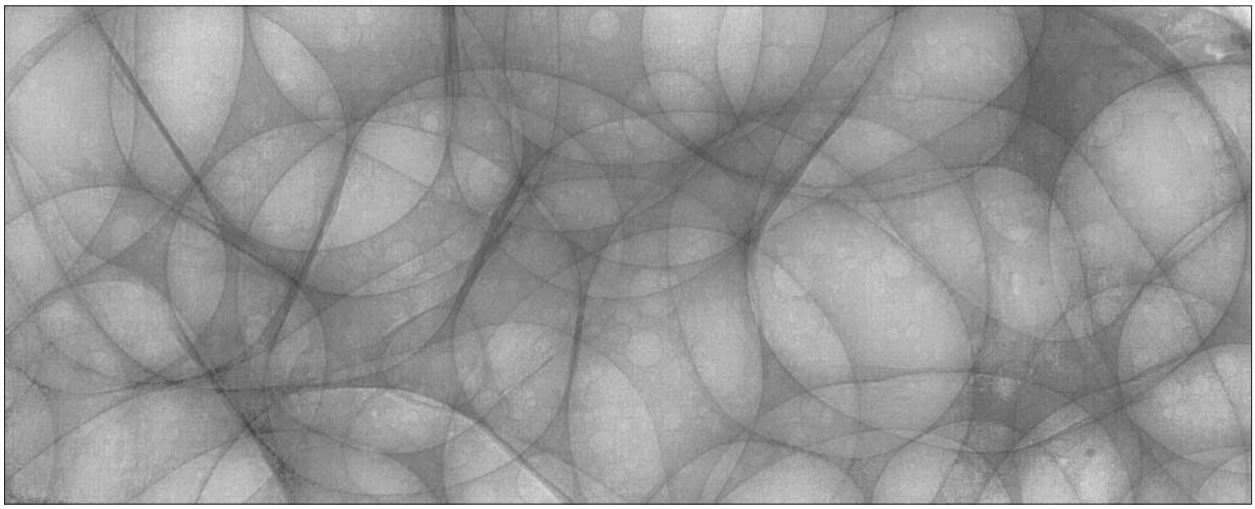

Fig. 1: X-ray radiograph of an evolving metallic foam taken with an exposure time of 600 μs

Radiography with penetrating rays can help to visualize the structure of opaque materials (Fig. 1). To study time dependent phenomena we need a series of radiographies, known as radioscopy. X-ray tubes can be used to study these phenomena, e.g., to visualize oxide films during solidification of aluminium alloys, growth of hydrogen pores in aluminium castings, or convective flow in liquid metals. However, the flux of conventional x-ray sources limits both the accessible frame rates to a few frames per second and spatial resolutions to some 10 μm. Thus in order to study processes in higher spatial and temporal resolution synchrotron radiation is applied.

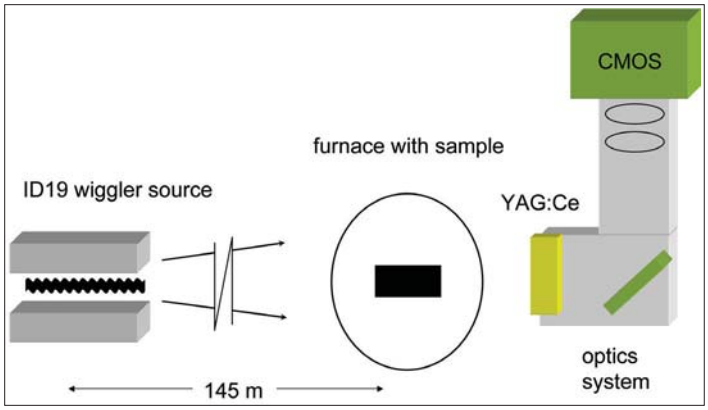

Fig. 2: Sketch of the fast imaging setup used on the ESRF's ID19 beamline

X-ray radioscopy, and especially synchrotron radioscopy, has gained considerable importance for the in-situ examination of evolving metallic foams within the last decade [1]. A common phenomenon in metal foams is coalescence. Thermal or mechanical instabilities lead to the rupture of a film separating two adjacent bubbles and their subsequent merger. It is important to understand the dynamics of these rupture events because they reflect the properties of the constitutive liquid. It has been estimated that these ruptures take place on a time scale of a few milliseconds or even faster. To image them, a very high frame rate is required.

We conducted an investigation of liquid metallic foams by means of high-speed radioscopy and captured 5000 images/s to reveal the details of pore coalescence during growth of Al-6%Si-4%Cu (wt. %) alloy foam [2]. Imaging experiments were carried out using the ID19 beamline at the European Synchrotron Radiation Facility, ESRF. A quasi-white spectrum of ID19's wiggler (gap 40 mm) was used in order to achieve the flux of $\approx 10^{15}$ photons/mm^{2}s required for our fast imaging application. The beam was filtered by 1.5 mm

of aluminium (including the two pressure vessel walls). We chose a PCO (10-bit dynamic range, 60 dB, 12 µm pixel size) as the fast camera. In order to reach the required 5000 frames/ s (200 ms exposure time), we restricted the region of interest to 1280×128 pixels. Fig. 2 shows a sketch of the setup.

The metal foam furnace setup utilised for the experiments consists of a ceramic heating plate placed inside an Al-cylinder (wall thickness: 0.5mm). This cylinder is closed tightly at both ends allowing vacuum and overpressures of up to 10 bar, with connections for heating current, thermocouple and gas in- and outlet. The system is described by the authors in detail in the literature [3].

The furnace was loaded for the experiments with a foamable Al-6%Si-4%Cu + 0.5 wt.% TiH_2 precursor measuring 10 x 5 x 4 mm^3, closed and placed in the beam path. Then it was filled with Ar up to 5 bar and the sample heated up at 25-30 K/s to T = 600°C. After melting, the gas contained in the blowing agent nucleates in the sample leading to a small expansion of ~ 5 – 10%. The pressure in the furnace is then decreased to normal by releasing the gas, a process called Pressure Induced Foaming (PIF) [4] which takes about 5 seconds. During this time, the camera records the foam evolution. The quick expansion produced by the pressure release accelerates the kinetics of foaming, leading to an increased occurrence of cell wall ruptures. The reason for using this method is to increase the number of ruptures during foaming to several hundred (by comparison with around 0-5 ruptures/s in standard foaming) in order to gather enough statistics during the limited measurement time of a few seconds.

In Fig. 3 we can observe the rupture procedure of a cell wall in an Al-6%Si-4%Cu foam in detail. The pore diameters of the foam are in the range of ca. 1-5 mm. The time interval between 2 consecutive images is 200 µs, leading to the total rupture and formation of a new cell wall in t_r = 600±100 µs. The diameter of the bubbles in question is in the range of 3 mm.

Of course, radioscopy does not reveal the true position of all the material and, therefore, we cannot specify how the rupture event was initiated and where exactly the metal in the ruptured features has been redistributed. But by a simple calculation we can affirm that during rupture, viscosity plays a minor role compared to liquid film inertia [2]. In this case, the liquid movement is largely dominated by inertia. This shows that the time taken for individual films to break suggests that the effective viscosity is that of the pure liquid within one order of magnitude.
In the literature, it has been proposed that a foam-stabilizing mechanism may be achieved via dramatically enhanced viscosity which is caused by the formation of a filigree network of oxides forming a gel. It has been found that an apparent viscosity of 400 mPas is the reason for the observed stability of foam columns. With such a high value for viscosity, viscous damping would lead to measurably higher values for t_r. A network of oxide fragments, clearly discernible in microscopic images of solidified foams, might give rise to high viscosity in an undistorted state and block liquid flow out of the films. After rupture, however, this network seems to have broken up. The viscosity of the liquid in the film appears to depend strongly on the history of the melt and the forces acting on it.

In conclusion, using white synchrotron x-ray radiation, a suitable fluorescent screen, and a fast CMOS camera, x-ray image sequences comprising up to 5000 frames/s can be acquired. The temporal evolution of the rupture of an individual metal film within a metallic foam was observed. The observed rupture time of about 600±100 µs is in agreement with a simple model that assumes inertia-limited film rupture and expresses the fact that the liquid in rupturing films is very fluid and behaves like a conventional melt.

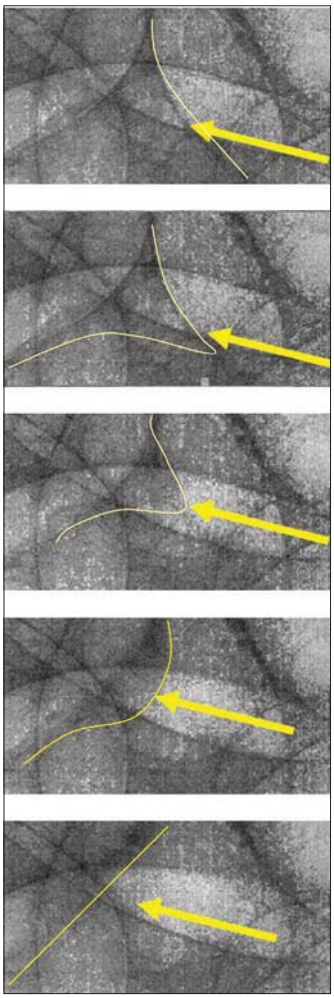

Fig. 3: Radiographs of a metal foam featuring a rupturing film. Images are 200 µs apart. The yellow line denotes the position of the rupturing film.

[1] H. Stanzick, M. Wichmann, J. Weise, L. Helfen, T. Baumbach, J. Banhart, AEM 4 (10), 814 (2002)
[2] F. García-Moreno, A. Rack, L. Helfen, T. Baumbach, S. Zabler, N. Babcsán, J. Banhart, T. Martin, C. Ponchut, M. Di Michiel, APL 92 (13), 134104 (2008)
[3] F. García-Moreno, N. Babcsan, J. Banhart, Col. & Surf. A, 263/1-3, 290 (2005)
[4] F. Garcia-Moreno, J. Banhart, Foaming of blowing agent-free aluminium powder compacts, Colloids and Surfaces A, Vol. 309/1-3, 264 - 269 (2007)

Corresponding author:
F. Garcia-Moreno
garcia-moreno@helmholtz-berlin.de

Relationships between structure and dynamics in hydrogen bonds of biopolymers

Heloisa N. Bordallo[1], Paulo de Tarso C. Freire[2], Elena V. Boldyreva[3], Dimitrios N. Argyriou[1], Antonios Kyriakopoulos[1]

■ 1 Helmholtz-Zentrum Berlin für Materialien und Energie, Berlin, Germany

■ 2 Departamento de Física, Universidade Federal do Ceará, Fortaleza, Brazil

■ 3 Novosibirsk State University, Institute of Solid State Chemistry and Mechanochemistry RAS, Russia

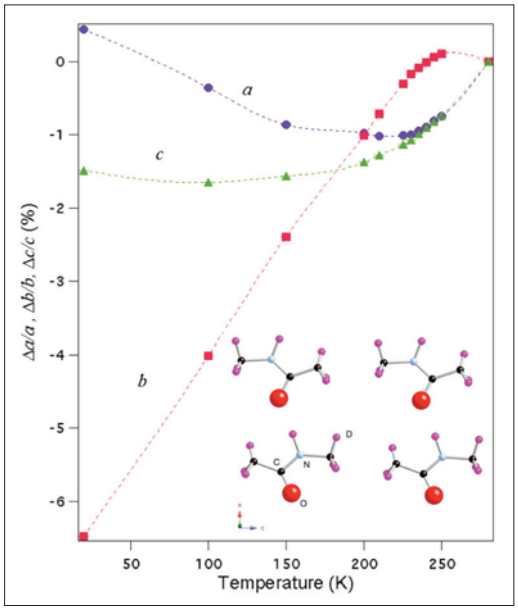

Fig. 1: NMA is built with 1D H-bond chains between amide groups of neighbouring molecules, which may be viewed as a model system for proteins. The temperature variation of the lattice constants shows an interesting behaviour, in which the *a*-axis shows a negative thermal expansion, whilst in comparison the *c*-axis shows a weaker temperature dependence.

Hydrogen (H) occurs in all materials in organic chemistry and the life sciences, and neutrons are commonly used to characterise both molecular motions and conformational changes in these systems. The large incoherent neutron cross-section of H (σ_H) provides both dynamic information from inelastic neutron scattering (INS) experiments and high-quality structural information from neutron powder diffraction (NPD) measurements. This enables the characterisation of conformational modifications that define subtle changes in the structures of bipolymers.

One part of our research focused on model systems for the peptide linkage in polypeptides and proteins. Simplistically, HBs can be explained by the electrostatic attraction between the partial charges on the atoms involved. By combining NPD with INS measurements, we have been able to associate the onset of a negative thermal expansion with a dynamical transition. One example of this is shown in Figure 1, where there is a non-linear increase of the atomic fluctuations around 230 K in N-methylacetamide (NMA). On cooling the O-H distance decreases, and causes intermolecular repulsive forces to increase; and it can be speculated that this triggers the lattice to relax, with the possibility of actual proton transfer at around 230 K[1] . Whilst further investigations are underway, this work shows the potential of NPD to determine structural deformations in small-molecular organic crystals.

Further studies were undertaken to understand the packing and conformation of amino acids. The structure-forming units in crystalline amino acids are similar to those in the biopolymers - head-to-tail chains of amino acids mimicking polypeptide chains; 2D layers mimicking β-sheets. The large σ_H means that a significant and significant background is often observed in diffraction patterns. To circumvent this problem either selective or full deuteration is used. Our initial studies focused on the smallest chiral amino acid, L-alanine ($C_3H_7NO_2$). We performed a careful analysis of its structural parameters using NPD in order to elucidate the role of the HBs. To date, studies on the physical properties of L-alanine have been undertaken, indicating a dynamic Jahn-Teller effect due to charge-lattice coupling[2]. Using selective deuteration, we focused on the dynamics of the different parts of the molecule (see Figure 2). Our findings are striking: deuteration of L-alanine causes significant structural changes as a function of temperature. As the substitution of deuterons (D) for protons (H+) in HB materials gives rise to an increase in HB lengths[3], our results suggest distinctly different relative stabilities between hydrogenated and deuterated L-alanine[4].

Recently[5], we quantified the subtle volume changes due to minor modifications in the packing density that resulted from the decrease in intermolecular distances in the HB networks on crystalline glycine, ($C_2H_5NO_2$). Glycine is an example of a very small organic molecule that

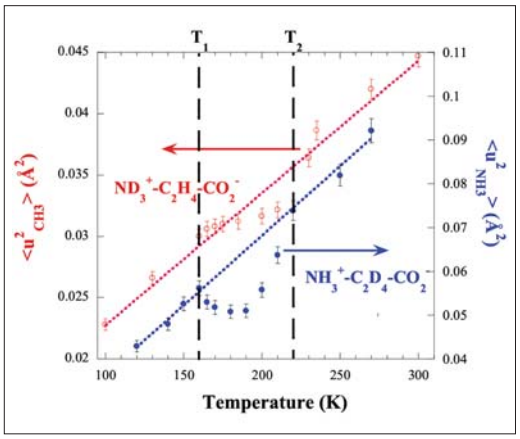

Fig. 2: Evolution of the deduced mean square dependence obtained from measurements using the time-of-flight spectrometer NEAT, as a function of the temperature for $ND_3{+}C_2H_4CO_2$- (left scale) and $NH_3{+}C_2D_4CO_2$- (right scale). The data suggests a structural rearrangement near 160 and 220 K.

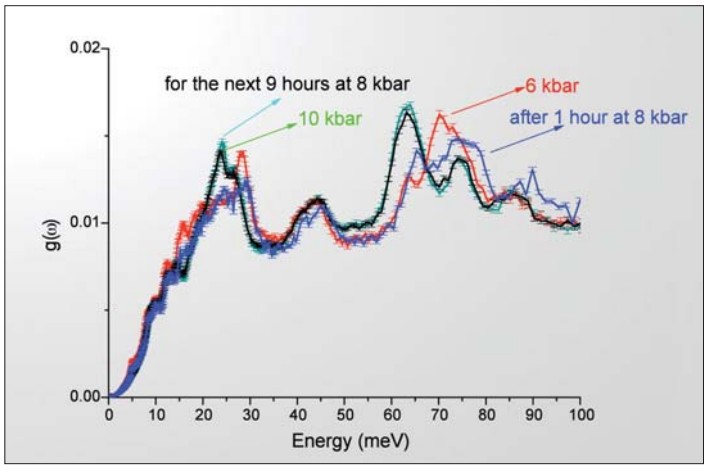

Fig. 3: Density of states for γ-glycine at 300 K as a function of pressure. The comparison of g(ω) measured at atm pressure and after release of the applied 10 kbar pressure indicates that the phase transformation is irreversible.

has several polymorphs, the stability of each depending on subtle changes in the crystallisation conditions and on the strength of the intermolecular HBs that link the head-to-tail chains of the zwitter-ions.

Our ambient pressure INS measurements showed that glycine polymorphs differ significantly in the phonon density of states, both in the positions of the bands and their relative intensities, despite there being only minor differences in molecular structure. The differences in stability of the polymorphs can be explained in terms of changes in intermolecular interactions and the high sensitivity of the conformation of individual molecules. We found that the mean-squared displacement dependencies reveal a change in dynamic properties at about 150 K for all three forms related to a reorientation of the NH_3-group. Besides, a clear and distinct response for the three polymorphs to high pressure was observed. The structure of the helical γ-polymorph was shown to be weak, although the molar volume was smaller than both the layered α– and β-forms. Stability of the α-form, as well as the polymorph transformations in β- and in α-glycine could also be demonstrated. Moreover, a pronounced kinetic effect was observed for γ-glycine: after the sample was kept at 8 kbar for one hour, a phase transition from a helical to a layered form occurred (see Figure 3). These experimental findings allowed us to relate the intermolecular HB response to the dynamic behaviour of the molecular fragments, explaining the ability of the structure to relax mechanically and form polymorphs.

This work has shown the potential use of neutron scattering to differentiate and elucidate biologically important molecules, albeit of small size. At present only molecules of less than 20 atoms have been studied, but we plan to extend this approach to molecules of greater size.

[1] H. N. Bordallo et al. J. of Phys. Chem. B 111, 7725 (2007)
[2] M. Barthès et al. EPJ B 37, 375 (2004)
[3] Such a change in the geometry of HBs is known as the Ubbelohde effect, J. Chim. Phys. 46, 429 (1949)
[4] J. M. de Souza et al. J. of Phys. Chem. B (Letters) 111, 5034 (2007)
[5] H. N. Bordallo, et al J. of Phys. Chem. B 112, 8748 (2008)
[6] http://www.julianvossandreae.com/index.html

Corresponding author:
Heloisa N. Bordallo
bordallo@helmholtz-berlin.de

Electrons suffer from the heat in an ion track

G. Schiwietz[1], M. Roth[1], K. Czerski[1,3], F. Staufenbiel[1], and P.L. Grande[2]

■ 1 Helmholtz-Zentrum Berlin für Materialien und Energie, Berlin, Germany ■ 2 Instituto de Física, Universidade Federal do Rio Grande do Sul, 91501 - 970, Porto Alegre, RS, Brazil ■ 3 Institute of Physics, University of Szczecin, ul. Wielkopolska 15, 70-451 Szczecin, Poland

A team of physicists from Germany and Brazil found that the absorption of fast electrons escaping from hot regions inside solids is significantly influenced by electronic heat - similar to what happens to long-distance runners who slow down or may even stop as a result of excessive heat.

In previous experiments at HMI, it had been shown that individual fast heavy ions may heat up the electrons in their close proximity (the so-called ion track) up to 80 000 K [1]. Such high temperatures were confirmed by independent experiments at the GANIL accelerator [2]. The physical picture that is consistent with most previous investigations is shown in Figure 1 [3]. Target ionisation destroys the bonds and yields hot electrons. Both facts give rise to atomic motions and subsequent materials modifications. Using atomic force microscopy, for example, it is possible to distinguish different depths of origin in the production of nano-structures (crater holes and crater rims) at the surface [4], but the role of hot electrons cannot be directly extracted from such structural measurements.

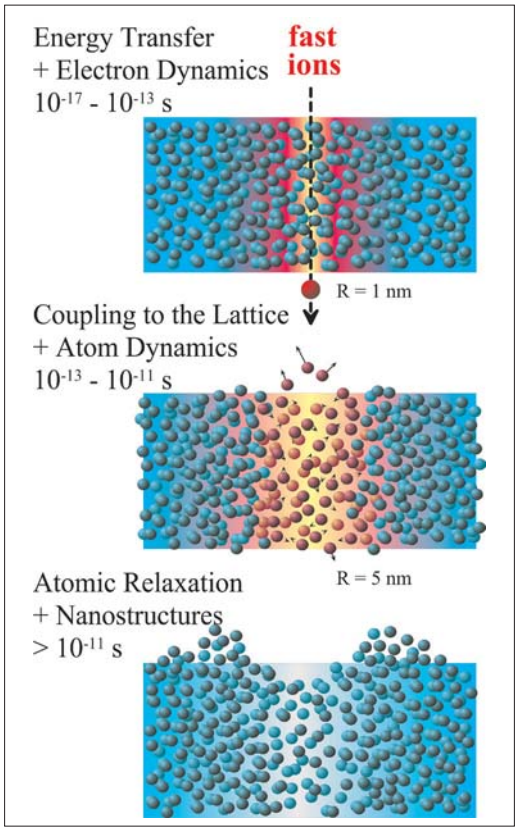

Fig. 1: Time evolution of an ion track [3]. The initial ionisation of atoms induces atomic motions which freeze out and may lead to permanent changes. In the bulk, this may lead to structural or chemical modifications. At the surface, craters or blisters on an atomic scale may also be produced.

So far, electron temperatures at the very centre of ion tracks have been extracted from the shape of Auger spectra [1-3]. The interaction of the escaping electrons with the hot electrons inside the track, however, might also influence the angular distributions. Figure 2 displays the setup for in-situ Auger energy and angular distribution measurements. Experiments have been performed with incident ions and electrons, both at 8% of the speed of light, using aluminum and beryllium samples always at normal incidence.

Figure 3 shows typical Al spectra after background subtraction and decomposition into L-Auger lines, corresponding to one (L^1VV) up to five (L^5VV) L-shell vacancies. Theses L-holes are filled by the interaction of two valence electrons. Already the existence of strong multiple inner-shell components indicates that practically all atomic bonds will break inside a heavy ion track. The L^nVV-lines for incident electrons have been normalised to the ion-peak maxima in the plot. The high-energy edge of the lines for incident ions is slightly broadened, consistent with high electron temperatures [3].

Figure 4 displays the Auger intensity (integrated around the peak maxima in Figure 3) versus ejection angle. Such angular distributions are known to be largely independent of the type of excitation, following roughly a cosine law. In Figure 4 the Auger intensities for two and three L vacancies (L^2VV and L^3VV) have been divided by the main line intensity $I(L^1VV)$ as a reference [5]. Thus, we predicted a constant intensity ratio $R_n = I(L^nVV)/I(L^1VV)$ which was, in fact, seen for R_2 and incident electrons, but clearly not for primary ions. For $I(K^2VV)/I(K^1VV)$ in the case of 592-MeV Au^{46+} + Be, we also determined a decreasing ratio for Auger emission angles close to 180° (for backward emission along the ion track) [5].

These decreasing intensity ratios are consistent

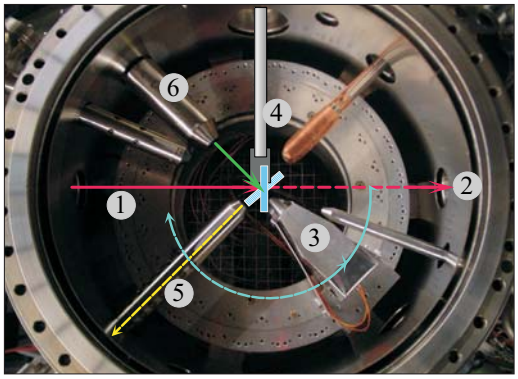

Fig. 2: Doubly magnetically shielded ultra-high vacuum chamber. The ion beam (1) from the ISL-cyclotron enters from the left and hits either the Faraday cup (2) or the target at normal incidence (4). The electron spectrometer (3) can be rotated around the target, after retracting the ion-mass analyzer (5). An electron gun (6) delivers a reference beam on the tilted target (at normal incidence).

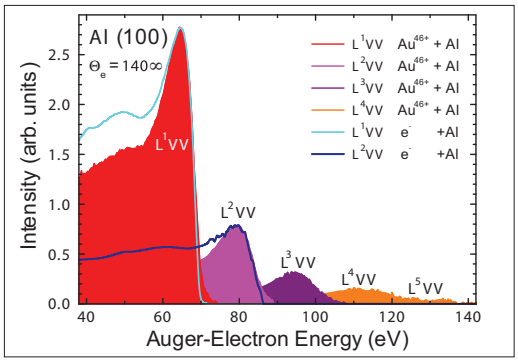

Fig. 3: Decomposed Auger-spectrum (colored areas) determined for 592-MeV Au^{46+} + Al at an electron-emission angle of 140° with respect to the beam direction. The separated peak structures for the L^nVV-Auger transitions represent different degrees of L-shell ionization. The blue and cyan curves show corresponding spectral shapes for incident electrons.

with enhanced electron absorption (enhanced inelastic electron-energy losses) of Auger electrons at high electron temperatures. High degrees of L-shell ionisation correspond to reduced Auger decay times (e.g., $5{\cdot}10^{-15}$ sec for L^3VV instead of $15{\cdot}10^{-15}$ sec for L^1VV), and the corresponding high averaged electron temperatures can exceed twice that for single L-shell vacancies. This broadens the Fermi-Dirac distribution and, consequently, Pauli-blocking effects lose importance when fast electrons move along the track during its high temperature phase.

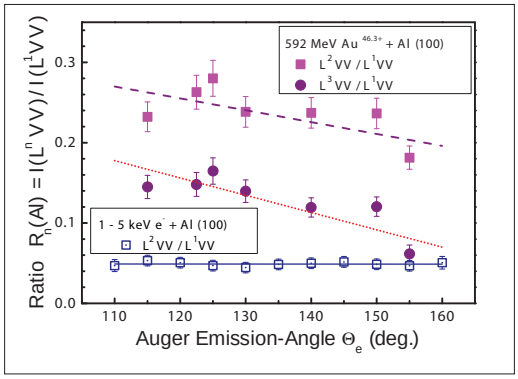

Fig. 3: Angular distribution of the Al-Auger line-intensity ratios for some L^nVV transitions. The straight lines represent error-weighted linear fits and show an unexpected decrease for heavy ions and large angles.

In conclusion, it has been demonstrated that Auger intensity ratios for different degrees of inner-shell ionisation vs. angle are sensitive to the high energy-deposition density. The results indicate that the transport of fast electrons is probing the spatial electronic excitation distribution inside ion tracks.

This work was supported by CNPq, CAPES, Humboldt Foundation and DAAD. We should also like to thank the ISL accelerator crew for delivering the necessary high quality heavy ion beams.

[1] G. Schiwietz, G. Xiao, P.L. Grande, E. Luderer, R. Pazirandeh, U. Stettner; "*Determination of the electron temperature in the thermal spike of amorphous carbon*", Europhys. Lett. 47, 384-390 (1999).
[2] M. Caron, H. Rothard, M. Beuve, B. Gervais, Physica Scripta T92 (2001) 281.
[3] G. Schiwietz, M. Roth, K. Czerski, F. Staufenbiel, and P.L. Grande; "*Femtosecond Dynamics – Snapshots of the Early Ion-Track Evolution*", Nucl. Instr. Meth. B226 (2004) 683–704.
[4] R.M. Papaléo, M.R. Silva, R. Leal, P.L. Grande, M. Roth, B. Schattat, and G. Schiwietz; "*Direct evidence for projectile charge-state dependent crater formation due to fast ions*", Phys.Rev.Lett. 101, 167601 (2008)
[5] G. Schiwietz, M. Roth, K. Czerski, F. Staufenbiel, and P.L. Grande; "*Indications for enhanced Auger-electron absorption in a hot electron gas*", Phys.Rev.Lett. 99, 197602 (2007).

Corresponding author:
G. Schiwietz
schiwietz@helmholtz-berlin.de

Ion-Induced Collective Rotation of Nanocrystals

I. Zizak[1], N. Darowski[2], S. Klaumünzer[2], G. Schumacher[2], J.W. Gerlach[5], W. Assmann[6]

■ 1 Berliner Elektronenspeicherring-Gesellschaft für Synchrotronstrahlung, Berlin, Germany ■ 2 Helmholtz-Zentrum Berlin für Materialien und Energie, Berlin, Germany ■ 3 Leibniz-Institut für Oberflächenmodifizierung e.V., Leipzig, Germany ■ 4 Ludwig-Maximilians-Universität Munich, Germany

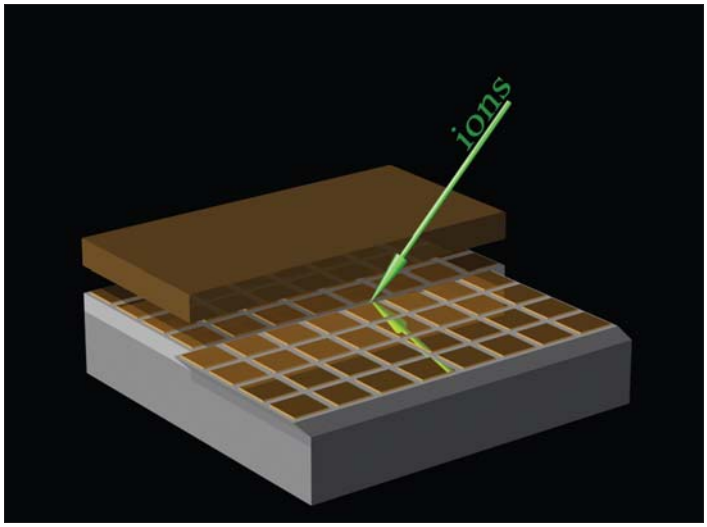

Fig. 1: Schematic view of the irradiation geometry for the detection of shear flow, by the observation of the shift of 20 nm thick gold squares relative to the unirradiated sample part. The shift occurs always in the direction of the projection of the beam onto the specimen surface.

In a solid, a fast heavy ion predominantly creates a trail of electronic excitations, along its straight trajectory. The excitation energy dissipates in the electronic system and is partly transferred to the atoms as a whole, so that on a timescale of 10^{-12} seconds a hot cylindrical ion track is generated, a few nanometers wide and many micrometers long. The lifetime of this thermal spike is between 10^{-11} and 10^{-10} seconds.

Can such tiny entities melt if the electronic excitation is sufficiently strong? A signature of the melting process is the relaxation of the thermo-elastic stresses toward the hydrostatic state. This stress relaxation gives rise to a relaxation strain, which is expected to be 'frozen-in' upon re-solidification. In amorphous materials this frozen-in relaxation strain leads to ion hammering: the dimensions of a free-standing thin specimen grow perpendicular to the ion beam whilst the dimension parallel to the beam shrinks, so that the mass density remains virtually unaltered [1,2]. An experimentally more convenient variant of ion hammering is shear flow in an irradiated layer on a radiation-inert substrate, when the ion beam and specimen normal subtend an angle $\theta \neq 0$ (Fig.1). By applying sufficiently long irradiation times, it is easy to achieve shear strains of $\gamma > 1$. Whilst ion hammering occurs in all amorphous materials, it has never been seen in microcrystalline substances which do not amorphise but remain crystalline during irradiation. The idea was that the dislocation loops, (which would constitute a plastic strain in crystalline matter) would be too small and hence spontaneously collapse and the thermal spike would disappear.

However, in the last three years of ISL accelerator operation, we detected shear flow in nanocrystalline ω-Ti and NiO [3]. Micrometer-thick layers of α-Ti with a pronounced (101) fibre texture have been produced by physical vapour deposition onto (100) silicon substrates. The layers were irradiated with 350 MeV Au ions at 300 K. The originally deposited α-Ti transforms below 1×10^{13} Au/cm^2 into ω-Ti. Figure 2 shows a micrograph of a ω-Ti layer (d = 2.7 μm, original grain size ≈

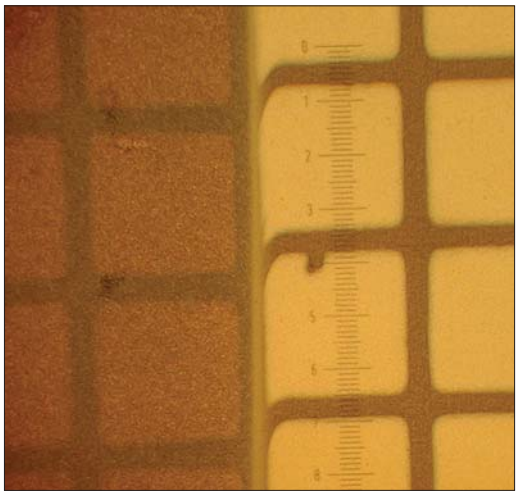

Fig. 2: Optical micrograph of ω-Ti, in which the right half side has been irradiated at 300 K with 350 MeV Au to 1.5×10^{15} Au/cm^2 with the geometry depicted in Fig. 1 ($\theta = 45°$). The arrow indicates the direction of the shift, which is 16.5 μm.

30 nm), where the right half has been uniformly irradiated with a fluence $\Phi t = 1.5\times10^{15}$ Au/cm^2 at $\theta = 45°$. From the surface shift of 16.5 μm, a shear strain of $\gamma = 3$ can be deduced. The situation is somewhat reminiscent to superplastic behaviour, where grain boundary sliding and grain rotation are important constituents. A measurement of the distribution of the crystallite orientations at the KMC-2 beamline at Berliner Elektronenspeicherring-Gesellschaft für Synchrotronstrahlung (BESSY) showed that the shear flow is accompanied by a tremendous collective rotation of the crystallites. In Figure 3 the average rotation angle is plotted versus ion fluence. The rotation angles are much larger than those observed previously during any other kind of material deformation. Changing the sign of θ reverses the direction of both flow and rotation as long as the crystallite size remains unaltered. With ω-Ti we started from nanocrystals whilst for NiO we started from single crystals of (100) or (111) orientation. At fluences ~1×10^{13} Au/cm^2 the single crystals fragmented

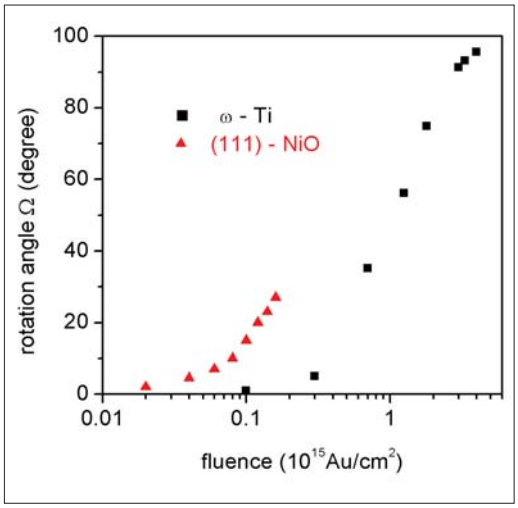

Fig. 3: Rotation angle of nanocrystalline ω-Ti and NiO grains versus ion fluence. The NiO was originally a single crystal with a (111) axis parallel to the surface normal.

into nanocrystals of about 30 nm in diameter. At larger fluences the nanocrystalline NiO exhibited grain rotation similar to ω-T, but the rotation rate (i.e. the rotation per incoming ion) is almost one order of magnitude larger (Fig. 3).

According to the experiments, shear flow and crystallite rotation are strongly coupled: the crystallites behave as if they were floating in an amorphous grain boundary matter and rotate nearly freely in the ion-induced shear velocity field. Amorphous grain boundaries undergoing ion hammering can semi-quantitatively account for this finding [3]. In this scenario grain rotation and shear always remain coupled and stop at large fluences, when grain growth leads to a continuous decrease of the amorphous grain boundary matter. However, the transition from a single crystal to an assembly of nanocrystallites as in NiO cannot be explained by this model.

Another scenario [3] assumes a stream of dislocation loops generated by shear stress relaxation in the ion tracks. Clustering of these dislocation loops in cell walls provides the starting point for the formation of grain boundaries and crystal fragmentation [4]. Subsequently generated dislocations pile up at grain boundary triple points and lead to moving disclination dipoles in the grain boundaries, which couple rotation and shear [5]. Disclination dipoles are specific arrays of dislocations and may play a role in nanocrystalline substances but not in microcrystalline ones [5]. In this scenario stopping of grain rotation without concomitant stopping of shear would occur when the crystallites are oriented such that a direction of easy glide coincides with the shear direction.

[1] S. Klaumünzer and G. Schumacher, Phys. Rev. Lett. 51 (1983) 1987.
[2] H. Trinkaus and A.I. Ryazanov, Phys. Rev. Lett. 74 (1995) 5072.
[3] I. Zizak, N. Darowski, G. Schumacher, J.W. Gerlach, and W. Assmann, Phys. Rev. Lett. 101 (2008) 065503.
[4] P. Hähner, K. Bay, and M. Zaiser, Phys. Rev. Lett. 81 (1998) 2470.
[5] I.A. Ovid'ko, Science 295 (2002) 2386.

Corresponding author:
S. Klaumünzer
klaumuenzer@hmi.de

Spin canting and orbital driven change of exchange pathways in the quasi one-dimensional frustrated chain material CaV_2O_4.

O. Pieper[1,2], B. Lake[1,2], A. Daoud-Aladine[3], M. Reehuis[1,4], K. Prokeš[1], B. Klemke[1], K. Kiefer[1], J. Q. Yan[5], A. Niazi[5], D. C. Johnston[5], A. Honecker[6]

■ 1 Helmholtz-Zentrum für Materialien und Energie, Berlin, Germany ■ 2 Technische Universität Berlin, Germany ■ 3 ISIS Facility, Rutherford Appleton Laboratory, Chilton, Didcot, UK ■ 4 Max Planck Institut für Festkörperphysik, Stuttgart, Germany ■ 5 Ames Laboratory and Department of Physics and Astronomy, Iowa St. University Ames, USA ■ 6 Universität Göttingen, Institut für Theoretische Physik, Göttingen

Low dimensional and frustrated magnetism appears in materials, where magnetic ions are arranged within the crystal lattice in such a way, that long-range order (LRO) caused by interactions between the ions cannot be established. Such quantum magnets attract a great deal of interest, since their ground states and spin dynamics differ significantly from bulk magnets [1]. The quasi-one-dimensional frustrated antiferromagnet CaV_2O_4 is from particular interest, since it possesses an additional orbital degree of freedom. By developing orbital order, this material can relax the frustration, giving rise the preferred exchange pathways.

CaV_2O_4 gains its magnetic properties from the V^{3+}-ions with two Hund-coupled electrons in the 3d-shell, leading to a total spin $S=1$. The material crystallises in the orthorhombic $CaFe_2O_4$-type structure at room temperature. The structure consists of double chains of edge-sharing VO_6 octahedra running along the crystallographic **c** direction. Within each chain the magnetic V^{3+} ions are arranged in a zigzag-like fashion with similar distances between nearest and next nearest neighbours. Since the dominant exchange mechanism is antiferromagnetic (afm) direct exchange, the underlying triangular motif is expected to give rise to geometrical frustration (Fig. 1) [2, 3]. In addition, the octahedral crystal field splits the 3d-levels, making the triply-degenerate t_{2g} orbital states accessible to the two electrons. However this orbital degeneracy is potentially lifted by distortions in the octahedral environment.

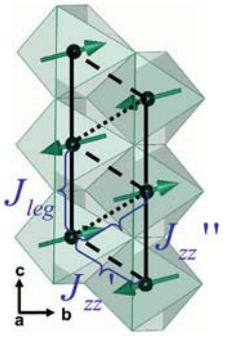

Fig. 1: The magnetic structure of CaV_2O_4. The V^{3+}-ions (black spheres) are located in the centres of the VO_6 octahedra. The arrows indicate the direction of the spin moments and the intrachain exchange constants are labelled. At high temperatures $J_{zz}' = J_{zz}''$.

To understand the complex physics of CaV_2O_4, both neutron diffraction and high temperature static susceptibility measurements were performed on single crystals. The DC magnetic susceptibility was measured at MagLab/LaMMB, Helmholtz-Zentrum Berlin (HZB), using a Quantum Design Physical Properties Measurement System. The temperature dependent susceptibility for a magnetic field applied along all main crystal axes is shown in Figure 2. The data shows the onset of afm LRO below $T_N=71$ K with the **b** axis being the easy axis. Interestingly a substantial finite susceptibility remains along this axis even to the lowest temperatures, possibly due to quantum fluctuations and/or spin canting. Furthermore, the data reveal a broad maximum around 270 K and a Curie-Weiss fit gives a Curie temperature of 418(5) K which is substantially higher than the Néel temperature [4]. Both results are indicators of low-dimensional and/or frustrated behaviour. To gain further information about the exchange interactions and the degree of frustration, exact diagonalisation (ED) calculations of a spin-1, one-dimensional Heisenberg model with nearest (J_{zz}) and next nearest neighbour (J_{leg}) exchange interactions (Fig. 1) were performed and the results were fitted to the high temperature data ($T>200$K) (see inset Figure 2). Surprisingly the best fits were obtained for solutions with either J_{zz} as the dominant coupling (and weak J_{leg}) or vice versa, rather than for approximately equal and frustrated couplings. Therefore, the ED fit suggests a single chain model at high temperatures.

To elucidate this issue and to clarify which mechanism relaxes the spin frustration it is essential to get detailed information about the magnetic structure. Thus, single crystal neutron diffraction experiments were performed using E4 and E5 at HZB and the Single Crystal Diffractometer (SXD) at ISIS. The data revealed that CaV_2O_4 undergoes an orthorhombic to monoclinic structural phase transition at $T_S=137$ K, and that it develops afm LRO below $T_N=71$ K with magnetic Bragg peaks appearing at $(h,k,l) + (0,0.5,0.5)$ positions (Fig. 3). Due to the lowering of crystal symmetry all magnetic reflections are twinned, thus significantly increasing the level of complexity for extracting a detailed magnetic intensity list. Our final refinement reveals a collinear spin structure within each zigzag chain, with antiparallel alignment of successive V^{3+} spins

along the legs and alternating antiparallel-parallel alignment along the zigzags. Spins of neighbouring chains are canted with respect to each other by equal and opposite amounts from the **b** axis (Fig. 1).

Deeper insights into the exchange paths can be gained by relating these findings to possible orbital arrangements, as the antiferromagnetic direct exchange interactions between neighbouring V^{3+} ions arises from overlap of their occupied t_{2g} orbitals. Since there are two electrons and three t_{2g} levels it is important to know the orbital energy level diagram in order to know which orbitals are occupied and can contribute to the exchange paths. This can be achieved by inspection of the octahedral environment. In the high temperature orthorhombic phase, the VO_6 octahedra are compressed in such a way as to lower the energy of the orbital with lobes along the legs, this orbital is therefore occupied by an electron and J_{leg} is strong. The second electron is shared between the remaining two orbitals which have lobes along the zigzag direction; this partial occupancy suggests a substantially weaker J_{zz} interaction (Fig. 3). Based on these findings, it follows that the dominant exchange coupling obtained from fitting the susceptibility data is the one along the legs.

In the low temperature monoclinic phase, the two V^{3+} ions are shifted slightly and there are now two distances along the zigzags leading to two inequivalent interactions J_{zz}' and J_{zz}''. The transition also distorts the VO_6 octahedra in such a way that the orbital degeneracy is completely lifted and the two electrons fully occupy the two lowest lying t_{2g} orbitals while the third orbital is completely empty. Since antiferromagnetic direct exchange arises from overlap of occupied t_{2g} orbitals, the resulting orbital pattern can be simply deduced from the magnetic structure (Fig. 1a). We conclude

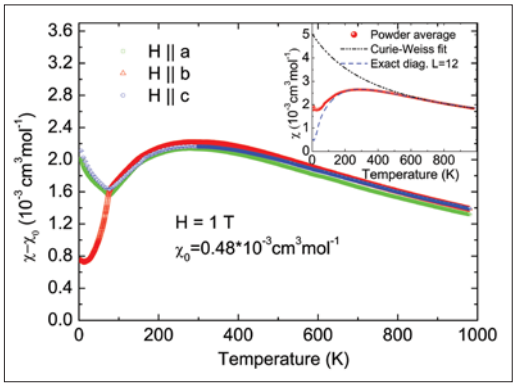

Fig. 2: Single crystal dc magnetic susceptibility of CaV_2O_4 along all crystallographic directions. The inset shows the powder averaged data fitted to Curie-Weiss and exact diagonalisation models.

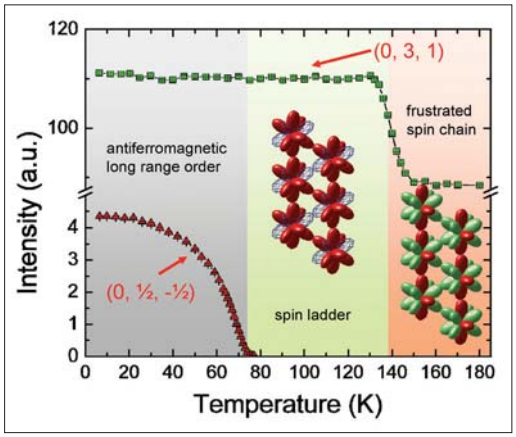

Fig. 3: Integrated intensity of magnetic (0, ½, - ½) and nuclear (0,3,1) Bragg peaks vs. temperature. The different background colours indicate different phases of the material. The insets show the orbital pattern occurring in the dedicated phases. Colour code: red; orbital fully occupied by one electron; green, orbital partially occupied by one electron; blue 'net', empty orbital.

that the J_{zz}'' interaction is weak and that the orbital with lobes along this exchange path is unoccupied, whilst the other two exchange paths are strong and the orbitals along these directions are fully occupied (Fig.3). The low temperature exchange paths are therefore completely unfrustrated and the structure can be interpreted as an S=1 spin ladder [4].

Our work shows the direct connection between orbital configuration and exchange paths and how a structural distortion can simultaneously relieve both orbital degeneracy and magnetic frustration, and can give rise to new magnetic structures.

[1] U. Schollwöck, J. Richter, D. J. J. Farnell, and R. F. Bishop, eds., *Quantum Magnetism, Lecture Notes in Physics*, vol. 645 (Springer, 2004).
[2] H. Kikuchi, M. Chiba and T. Kubo, Can. J. Phys. 79, 1551 (2001)
[3] A. Niazi, S. L. Bud'ko, D. L. Schlagel, T. A. Lograsso, J. Q. Yan, D. C. Johnston, A. Honecker, R. W. McCallum, M. Reehuis, O. Pieper, B. Lake, A. Kreyssig, Phys. Rev B 79, 104432 (2009)
[4] O. Pieper, B. Lake, A. Daoud-Aladine, M. Reehuis, K. Prokeš, B. Klemke, J. Q. Yan, A. Niazi, D. C. Johnston, A. Honecker, cond-mat/0812.1808(2008), accepted for publication in Phys. Rev. B

Corresponding author:
O. Pieper
oliver.pieper@helmholtz-berlin.de